40th Fluid Dynamics Conference and Exhibit
28 June - 1 July 2010, Chicago, Illinois

AIAA 2010-4447

Numerical Study of Laser-Spot Effects on Boundary-Layer Receptivity for Blunt Compression-Cones in Mach-6 Freestream

Yuet Huang[1] and Xiaolin Zhong[2]
University of California, Los Angeles, California, 90095

This paper presents the direct numerical simulation (DNS) study of the boundary layer receptivity for blunt compression cones in Mach-6 flow with freestream laser-spot (hotspot) perturbation. The flow conditions are the same as the Boeing/AFOSR Mach-6 Quiet tunnel (BAM6QT) in Purdue University. Compression-cone geometry is expected to cause laminar/turbulence transition in shorter stream-wise distance than straight-wedged cone geometry due to adverse pressure gradient occurs along the body. Therefore, using compression cones is advantageous to study the transition mechanisms. The DNS will be carried out in two parts: simulation of the steady flow behind the bow-shock, and simulation of the unsteady flow behind the bow-shock. The aim of the DNS is to generate the results that are agreeable with Purdue's laser induced hotspot experiment for compression cones.

Nomenclature

M_∞	=	freestream Mach number
ρ_∞	=	freestream density
T_o	=	total temperature
T_{wall}	=	temperature at the wall
γ	=	ratio of specific heat
Pr	=	Prantl number
R	=	gas constant
μ_r	=	reference viscosity coefficient
T_r	=	reference temperature
T_s	=	Sutherland's temperature
T_∞	=	freestream temperature
e	=	total energy per unit volume
q_j	=	heat flux due to thermal conduction
τ_{ij}	=	shear stress tensor
$\frac{\mathrm{Re}_\infty}{L}$	=	freestream Reynolds number per unit length

I. Introduction

Boundary layer receptivity is the process for the environmental disturbances enter the boundary layer and generate instability waves. Also, boundary layer receptivity is a preliminary process for the occurrence of laminar-turbulent transition [2, 8]. In hypersonic flow around a blunt body, the curved bow-shock wave creates entropy and vorticity layers, which will be swallowed by the boundary-layer [8]. Moreover, there exists interaction between freestream perturbations and the bow-shock, which would create significant influence toward the boundary layer receptivity behind the bow-shock. Therefore, extensive study of boundary layer receptivity under various perturbations and body geometry effects is extremely important for accurately predicting the laminar-turbulence transition location on blunt bodies such as aerospace vehicles. One of the reasons that make the accurate prediction of hypersonic boundary layer transition location highly necessary is that transition can cause extremely high temperature at the vehicle surface, which may lead to devastating disaster. However, nowadays the mechanisms behind hypersonic laminar-turbulence transition are still not being thoroughly understood.

Compression cone (see Figure 1) is a circular-base cone with circular-arc geometry along its body in longitudinal direction. Such compression geometry was expected to cause laminar-turbulence transition under quiet-flow conditions due to adverse pressure gradient acts along the longitudinal curvature of the cone [5, 7]. The aim in

[1] Graduate Student, Mechanical and Aerospace Engineering Department.
[2] Professor, Mechanical and Aerospace Engineering Department, AIAA Associate Fellow.

designing such geometry of the compression wall is to create constant thickness boundary layer that has continuous amplification of a narrow range of instability frequencies [5].

Schneider et al [5], has performed both numerical analysis and experimental instability measurements on the compression cones. In their numerical analysis, they have used STABL software, which implement shock-capturing scheme to simulate the flow around compression-cones in steady Mach-6 freestream. And the computed steady flow solutions were analyzed by the Linear Stability Theory (LST) and Parabolized Stability Equations (PSE) analysis. Their LST results indicate that the maximum N-factor of 16 at the aft end ($x \approx 0.45m$) of the compression cone. In their Mach-6 wind tunnel experiments, they have measured the second-mode instability under quiet and noisy flows.

In 1998, Dunn [1] has performed numerical simulation on the flow past a hemisphere with hotspot in freestream. Dunn has used commercial code INCA, which implements Steger-Warming flux-splitting finite-volume scheme with upwind-biased differencing in shock-capturing domain, for DNS of Navier-Stokes equations. Dunn has modeled the hotspot as an energy pulse imposed in a cell of the computational grid on the freestream stagnation line, and convected with the flow into the shock. However, the numerical simulated hotspot profile bears quite a difference to Schneider's laser-spot profile in previous experiment; the resonance effect in experiment cannot be confirmed by Dunn's numerical results. Dunn suspected that such discrepancy is caused by poor spatial resolution. Therefore, an idea of increasing grid density around the thermal spot region is raised. Salyer et al suspect that the discrepancy is also due to poor temporal resolution in simulating the propagation and diffusion of the hotspot [3, 4]. However, one should also consider that the dissipative feature of Steger-Warming flux-splitting scheme may also be the possible cause of the discrepancy. In his results, he found vortex-rings and pressure waves in the subsonic region behind shock [1].

In 2004, Zhong [7] has computed the mean flow simulation of a blunt cone with combined straight and compression wall. Its nose radius is 0.0015875 m, and the half angle is 5 degrees. His mean flow results are validated with experimental results, and can provide a qualitative reference to the results that are presented in this paper.

Kovasznay [11] stated that the weak disturbances in compressible flow can be decomposed into acoustic, entropy and vorticity disturbance. McKenzie et al. [10] stated that regardless of the type of disturbance, its interaction with the shock always generates acoustic, entropy and vorticity disturbances behind the shock. However, the mechanisms of the interaction between different types of disturbance to the shock are individually different, which would lead to difference in intensity and travelling angle of the disturbances behind the shock. In reality, the disturbances exist during flight in atmosphere consist all three kinds. Therefore, a comprehensive study of all three types of freestream disturbance-shock interactions is necessary for a complete analysis on hypersonic boundary layer receptivity study over blunt body. Receptivity study of freestream acoustic disturbance and shock interaction over blunt body has already been studied much in experiments, DNS and theories [3, 4]. And, using laser to generate hotspot is a feasible way for imposing freestream disturbance other than acoustic disturbance in wind tunnel experiment [3, 4]. Hence, it is suitable to use hotspot as the freestream perturbation in this paper.

The numerical simulation study that is presented in this paper is divided into two parts: (i) mean flow simulation and linear stability analysis, and (ii) effect of hotspot perturbation/bow-shock interaction to the boundary layer receptivity. For both parts, there exist stages for completing the perspectives of the study.

In part (i), the first stage is to compute steady flow solutions for different nose bluntness cases. Steady flow solutions can be used to perform LST analysis as the second stage, so as to validate the numerical simulation with Purdue's numerical results.

In part (ii), the first stage is to simulate the unsteady flow by imposing a sinusoidal entropy wave in upstream of the bow-shock on the stagnation line, so as to validate the correctness of the computer code for imposing disturbances onto the mean flow. The second stage is to simulate the unsteady flow by imposing a hotspot in upstream of the bow-shock on the stagnation line. In the future, the hotspot flow solutions will be compared with Purdue's wind-tunnel laser-spot experiment results.

II. Governing Equations and Numerical Methods

The governing equations for DNS of hypersonic perfect-gas flow around compression cone are the following three-dimensional Navier-Stokes equations in conservative-law form and Cartesian coordinates:

$$\frac{\partial U}{\partial t}+\frac{\partial F_j}{\partial x_j}+\frac{\partial F_{vj}}{\partial x_j}=0,\ \ j=1,2,3\,.$$

Vector U contains five conservative-law form dimensional flow variables:

$$U = \begin{bmatrix} \rho & \rho u_1 & \rho u_2 & \rho u_3 & e \end{bmatrix},$$

F_j and F_{vj} are the vectors of convective (inviscid) flux and viscous flux in jth spatial direction respectively:

$$F_j = \begin{bmatrix} \rho u_j \\ \rho u_1 u_j + p\delta_{1j} \\ \rho u_2 u_j + p\delta_{2j} \\ \rho u_3 u_j + p\delta_{3j} \\ (e+p)u_j \end{bmatrix},$$

$$F_{vj} = \begin{bmatrix} 0 \\ -\tau_{1j} \\ -\tau_{2j} \\ -\tau_{3j} \\ -\tau_{jk}u_k - q_j \end{bmatrix}, \quad k = 1,2,3$$

The equation of the state and the transport equations are:

$$p = \rho RT,$$

$$e = \rho\left(c_v T + \frac{1}{2}u_k u_k\right),$$

$$\tau_{ij} = \mu\left(\frac{\partial u_i}{\partial x_j} + \frac{\partial u_j}{\partial x_i}\right) - \lambda\frac{\partial u_k}{\partial x_k}\delta_{ij}, \quad \lambda = \frac{2}{3}\mu$$

$$q_j = -\kappa\frac{\partial T}{\partial x_j}$$

where R is the gas constant C_v and C_p are the specific heats that are assumed to be constant with a given specific heat ratio γ. κ is the heat conductivity coefficient, which can be determined with a constant Prantl number. The viscosity coefficient μ is defined by the Sutherland's law:

$$\mu = \mu_r\left(\frac{T}{T_0}\right)^{\frac{3}{2}}\left(\frac{T_r + T_s}{T + T_s}\right).$$

Throughout the DNS numerical method implementations, the Cartesian Navier-Stoke's equations have been transformed into body-fitted curvilinear computational domain coordinates (ξ, η, ζ) via Jacobian matrix. The computational domain is bounded by the bow-shock and the wall of the cone, which is called shock-fitting domain. Using shock-fitting method can accurately resolve the position of the bow-shock, which is necessary to obtain the high accuracy of the flow solutions for receptivity and stability analyses. The shock-fitting grids are moving-grids in time, and the motion is depended on the shock position and the shock velocity. In the each time-step, shock position and shock velocity are the unknowns, and would be solved by the before-shock conditions and behind-shock solutions. Spatial discretization of inviscid flux derivatives in stream-wise (ξ) and wall-normal (η) are done by using fifth-order finite-difference upwind schemes with local Lax-Friedrichs flux-splitting scheme, and sixth-order

central finite-difference scheme is used for viscous flux derivatives. For spatial derivatives in azimuthal direction (ζ), Fourier collocation method has been used. Runge-Kutta method is used for time-marching. The details of shock-fitting method, finite difference schemes, and other numerical method implementations of the DNS are shown in Zhong's paper [6].

III. Modeling Equations of Freestream Disturbances

Before starting simulate the hotspot bow shock interaction, first run a simple test case with sinusoidal wave in the freestream to validate the computer code. From Zhong's unsteady flared cone DNS paper [7], the modeling equation for general 2D single sinusoidal entropy wave that is imposed in the freestream can be derived. The amplitude of density disturbance is:

$$\Delta\rho = \varepsilon\rho_\infty,$$

where ε is amplitude factor. After adding the disturbance to the freestream density, the disturbed density in freestream becomes:

$$\rho = \rho_\infty + \Delta\rho q \cos\left(k_x x + k_z z - \omega t\right),$$

where the periodic frequency is:

$$\omega = kU_\infty \cos\varphi,$$

φ is oblique angle of the wave relative to x-axis, k is wave number, and k_x is x-component of wave number, k_z is z-component of wave number, q is perturbation factor.

In physics, the hotspot has Gaussian temperature or density distribution for its core region [3, 4]. Thus, Gaussian equation is used to model the hotspot in this paper. Since in Dunn's paper the initial position of the hotspot is 2cm upstream of the shock [1], for Mach-6 flow, the time scale for the hotspot to diffuse and propagate in freestream is extremely small compare to the length scale of the initial distance between center of hotspot and the shock. Therefore, it is reasonable to assume the hotspot profile remain steady when convecting with freestream. For 3D hotspot model, the perturbed freestream temperature is:

$$T = \Delta T_{\max} \exp\left(-\frac{R_c^{\,2}}{2\sigma^2}\right) + T_\infty,$$

Hence, by ideal gas law, the perturbed freestream density is:

$$\rho = \frac{p_\infty}{R\left(T_{\max} \exp\left(-\frac{R_c^{\,2}}{2\sigma^2}\right) + T_\infty\right)},$$

the time derivative of perturbed freestream density at shock location is:

$$\frac{\partial\rho}{\partial\tau} = \left(\frac{p_\infty}{\sigma^2 R}\right) T^{-2}\left(T - T_\infty\right)\left[\left(X_c - U_\infty t\right)\left(\frac{\partial X_c}{\partial\tau} - U_\infty\right) + y_{shk}\frac{\partial y_{shk}}{\partial\tau} + z_{shk}\frac{\partial z_{shk}}{\partial\tau}\right],$$

where σ is Gaussian shaping factor, τ is time in computational domain. X_{spot} is the initial x-coordinate of spot center. The initial x-coordinate difference between the shock location and the spot center is:

$$X_c = \left|X_{spot} - x_{shk}\right|,$$

x_{shk}, y_{shk}, z_{shk} are shock-front coordinates. By using the transport equation in mathematics, the distance between hotspot center and any point on the shock front at any time is:

$$R_c = \sqrt{\left(X_c - U_\infty t\right)^2 + y_{shk}^2 + z_{shk}^2}\,.$$

Please note that the time in computational domain is the same as the time in physical domain [6].

IV. Freestream Conditions and Compression Cone Geometries

The freestream conditions used in the numerical simulations in this paper is based on Purdue's Mach-6 Quiet Tunnel (BAM6QT) [5]:

$M_\infty = 6.0$
$\rho_\infty = 0.0403\ kg/m^3$
$T_o = 433.0\ K$
$T_{wall} = 300.0\ K$
$\gamma = 1.4$
$Pr = 0.72$
$R = 287.04\ Nm/kgK\ (air)$
$\mu_r = 1.7894 \times 10^{-5}\ kg/ms\ (sea\ level)$
$T_r = 288\ K\ (sea\ level)$
$T_s = 110.3333K\ (air)$
$\frac{\mathrm{Re}_\infty}{L} = 1.026 \times 10^7\ m^{-1}$

The compression cone geometry is based on Schneider's design [5]:

body-arc radius = 3.0 *m*
cone half-angle = 2.0 *degrees*
cone length $\approx$ 0.45 *m*

There are two cases designed to examine nose-bluntness effect on boundary layer receptivity:

Case 1: *nose radius* = 0.0127 *m* (0.5*in*)
Case 2: *nose radius* = 0.001 *m* (Purdue's)

Please note that case 2 is based on Schneider's compression cone nose radius, therefore the result can be compared with his numerical and wind tunnel experiment results.

V. Disturbances and Hotspot Parameters

The parameters of 1D sinusoidal disturbance are:

$\varepsilon = 0.005$
$q = 0.2582$
$k = 718.9$ radian/m
$\varphi = 0$ (for 1D)

Therefore, the wavelength is 0.008740 m and the periodic frequency, ω is 628319 radian/s.

There are three cases of different hotspot peak-region radius for DNS with hotspot perturbation. The peak radius is controlled by the Gaussian factor, σ:

Case A: $\sigma = 0.001$ (largest radius: r = 0.003 m), $X_{spot} = -0.02$ m
Case B: $\sigma = 0.00005$ (smaller radius: r = 0.0002 m), $X_{spot} = -0.0025$ m
Case C: $\sigma = 0.00003$ (smallest radius: r = 0.0001 m), $X_{spot} = -0.0018$ m.

These cases are all based on the mean flow solution of case 2, and in order to keep the disturbance linear in the flow, the maximum temperature perturbation amplitude is chosen to be:

$$\Delta T_{\max} = T_\infty \times 10^{-4} = 0.00528K.$$

Case A is referred to the actual hotspot parameters in Purdue's experiments [3, 4].

VI. Procedures and Simulation Results

All the flow variables shown in the figures are dimensionless, which are normalized by the corresponding freestream values. For all contour plots, the upper boundary is the location right behind the shock, the lower boundary is the cone-surface, and the right boundary is the exit boundary. Since the cone is at zero degree angle of attack, thus, only the upper half of the cone is displayed, and the lower half can be reflected by mirror image. Figure 3 demonstrates the computation grid structure around the cone. Since the computing power is relatively limited for computing almost a million grid points at once, the simulation is done in 18 zones. Zone 1 is the computation domain that wraps around the hemispherical cone nose, zone 2 to zone 18 wrap around the compression wall.

A. Steady Flow Solutions

Case 1 is designed to demonstrate the effect of having a very blunt nose for the compression cone. The contour plot of Mach number is shown in Figure 4. One can see the Mach-number boundary layer become thinner along stream-wise direction. The Mach number of the flow behind shock increases as going downstream. The contour plot of entropy is shown in Figure 5. One can see the entropy layer generated by the bow-shock nearby the cone nose become thinner when going downstream. The grid resolution for all case 1, 2 are $3720 \times 240 \times 4$.

Based on the observation of the Mach number boundary layer, one can see that the effect of blunt nose is far more significant than the effect of compression wall. The blunt nose is causing very large pressure in the flow field around the nose behind shock, and the pressure decreases by going further downstream, this is revealed by having increasing Mach number and attenuation of Mach-number boundary layer. Compression wall is designed to produce adverse pressure gradient, $\partial p / \partial \xi > 0$ in downstream direction. However, such effect cannot be revealed due to the absolute value of favorable pressure gradient, $\partial p / \partial \xi < 0$ that is caused by blunt nose, is larger than the absolute value of adverse pressure gradient that is caused by compression wall. Moreover, it can be predicted that if one repeats the simulation on a straight wedged cone with the same nose geometry and flow conditions in case 2, its pressure gradient in downstream direction will be more negative than the pressure gradient on compression cone.

Case 2 is designed to demonstrate the boundary layer receptivity when the bluntness effect is overall less significant than the effect of compression wall. The mean flow contour plots of pressure, temperature, entropy, density and Mach number are shown in Figure 6, 8, 9, 11 and 13 respectively. From the pressure contour, one can see that the pressure first decreases shortly behind the nose, then increases when going further downstream; the overall pressure gradient is increasing when going downstream. Such trend can be more precisely revealed by the plot of pressure along the wall in Figure 7, and it matches the expectation of using a compression cone. The temperature contour reveals the similar trend to the pressure; the temperature above boundary layer first decreases shortly behind the nose, then increases very gradually when going further downstream. This trend can be more precisely seen in the temperature profile at various downstream locations in Figure 16, 18, 20 and 22. Since the wall surface temperature is fixed, so in the temperature contour plot, there is a red colored layer right above the wall. From the entropy contour, one can see the entropy layer is generated around the blunt cone nose, and being swallowed by the boundary layer at further downstream. Density contour shows that the overall density increases when going downstream as a result of compression. Mach number plot and the Mach number profile at various locations in Figure 15, 17, 19 and 21 show that the Mach number increases for a short distance behind blunt nose, then decreases for a long distance in further downstream, where the adverse pressure gradient takes place.

Based on the observation of case 2 pressure contour or the pressure plot along the wall; there is a large recompression zone appearing after a short distance from the cone nose, one can conclude that the trend is opposite to case 1; compression wall effect is dominant in case 2, the effective distance of bluntness is very short. By comparing the density and Mach number contours of case 2 to Purdue's mean flow contours with the exactly the same cone geometry and freestream flow conditions, Figure 10 and 12 [5], one can see that the case 2 contours agree well with Purdue's contours that are computed by their shock-capturing program. More precise comparison can be seen by overlaying the case 2 shock front to Purdue's shock front in Figure 14. The roughness of Purdue's shock front data is due to the uncertainty of exact shock front location when implementing shock-capturing method. But still, both shock fronts match well.

In boundary layer linear stability theory (LST), N-factor is the exponential power index of the amplification rate A/A_0, the ratio of amplified disturbance amplitude to initial unamplified disturbance amplitude, namely $A/A_0=e^N$. The location of laminar-turbulence transition is empirically related to the critical values of N-factor. In low-noise wind tunnel, the typical critical N-factor for sharp cones is 8 to 11 [5]. Therefore, at any downstream location with N-factor larger than or equal to that critical range, the transition is most likely to take place over there. LST analysis in this paper is to include a small linear disturbance with different frequencies in the Navier-Stoke's equations of the

mean flow, and to compute the analytical solutions to the corresponding eigenvalue problems to get N-factors for each frequency [12]. The aim is to find the frequency that causes the maximum N-factor.

The significant adverse pressure gradient along the wall causes earlier boundary layer instability amplification occurrence when compare to straight wedge cone, thus, case 2 is the main focused case for receptivity study. LST analysis is performed in order to precisely validate case 2 mean flow results with Purdue's mean flow results. Schneider et al. has performed LST and PSE analyses on their mean flow [5]. There are five frequencies that are used in the LST analysis; they are being arranged from low to high. The third frequency in LST is different to the third frequency that is used in Purdue's PSE analysis, namely the LST one is 278996 Hz, and the one in PSE is 286100 Hz. Comparisons of LST results of case 2 to Purdue's LST and PSE results are shown in Figure 23 and 24, it can be seen that the results of highest four frequencies are close to each other, and the most amplified frequency in case 2 is 278996 Hz. Both results of the lowest frequency of case 2 appear lower than Purdue's results at farther downstream. However, LST results are very sensitive to the mean flow; an insignificant discrepancy in mean flow can lead to qualitatively incorrect LST results, and case 2 LST results are still qualitatively consistent with Purdue's results. Hence, case 2 mean flow results are consistent with Purdue's mean flow results.

B. Unsteady Flow solution with 1D Sinusoidal Entropy Wave

After the case 2 mean flow solutions are computed, an unsteady run for only the cone nose (zone 1) with one dimensional sinusoidal wave in freestream is aimed to validate the computer program and procedures that are used to simulate general unsteady freestream cases. Figure 25 and 26 show the time history of horizontal velocity perturbation and pressure perturbation along the stagnation line behind the shock nearby the wall respectively. The zone 1 grid resolution is $240\times120\times4$. In the computer program, j=1 is the grid index at the wall-surface, as j increases, the corresponding location of the grid node is marching towards the shock from the wall. As one can see from Figure 25, the amplitude of velocity disturbance is maximum at the nearest point to the shock, then decreases until hits the wall, it become zero, which agrees with no-flow-through boundary condition of solid wall. The amplitude of pressure perturbation is almost the same at all locations. The perturbation appears in sinusoidal form, which qualitatively validates the unsteady simulation.

C. Unsteady flow Solution with Hotspot Perturbation in Freestream

This stage is to include the effect of the interaction between freestream hotspot perturbation and bow-shock, to the behind-shock flow solution. The key to do this is to determine the unsteady freestream flow variables and their time derivatives at the shock position so as to calculate the velocity of shock front, then update the shock position, and then recalculate the flow variables behind the shock and their time derivatives, then update the unsteady freestream flow variables and their time derivatives at the new shock position again, that is completing one time step. Repeat such procedure with marching in time step until the perturbation completely passes through the computation domain.

See Figure 27 and 28 for case A temperature and density distribution in radial-direction in a 3D hotspot. These two plots are created along one axis in space, therefore, there are negative x coordinates at the left side of the origin. Since the 3D hotspot is a spherical distribution region, these plots represent the profile in any direction. One can see that the peak region radius of the hotspot in case A is around 0.003m.

Figure 29 shows the case A time history of hotspot entropy perturbation passes through the shock and convects toward the wall along the stagnation line. And Figure 31 shows the time history of entropy perturbation travels along the wall surface in zone 1. The zone 1 grid resolution for all case A, B, C is $240\times120\times4$. The legend indicates the schematic time steps; 't1' is the earliest time, 't2' is the next schematic time, and so on. The sizes of the schematic time steps are not uniform. From the stagnation line entropy time history, one can see the entropy perturbation passes into the shock, then moving toward to wall, while its amplitude is damping out. The wall entropy time history shows that it damps out at further downstream.

Figure 30 shows the time history of hotspot pressure perturbation along the stagnation line, and Figure 32 demonstrated the pressure perturbation travels along the wall surface in zone 1. Since the radius of the hotspot is relatively large compare to the nose radius, the acoustic effect of pressure perturbation is not clearly indicated in case A diagrams. Therefore, the smaller hotspot cases are designated to demonstrate the structure of the both entropy and pressure perturbations behind the shock. However, the hotspot parameters in case A are based on the size and the initial spot position in Purdue's laser spot wind tunnel experiments. Therefore, only case A results are being compared to the experiment results in the future.

The snapshot of a moving entropy spot is demonstrated in Figure 33. The red region is the peak of the hotspot, and it is travelling toward right-hand-side, and eventually passes through the right-most exiting boundary, and goes

into the next zone, namely zone 2. The snapshot of moving pressure perturbation is in Figure 34. The pressure peak has negative value.

Case B and Case C show the structure of the hotspot behind the shock more clearly. One can see the perfect Gaussian shapes in the entropy and pressure time history plots in Figure 35, 36, 39 and 40 respectively. From the entropy time history, the decay of the amplitude is very clearly shown. This is due to the diffusion and the viscous damping in the flow behind the shock. If the pictures of the pressure time history are in motion, one can more easily to see the pressure perturbation bouncing to and fro between the wall and shock, so called acoustic effect [10].

Figure 37, 38 and 41 are the snapshot of entropy and pressure perturbation in case B and C. It is very clearly shown the shape of spot in the flow behind the shock. However, since the radius of the spot in case B is 15 times smaller than case A, and case C is 30 times smaller than case A, the intensity of the perturbation in both cases are extremely weak compare to case A, the amplitude in case B and C damped out very soon before reaching the exit boundary, therefore it is not meaningful to show the amplitude plot along wall., but the stagnation line. Figure 41 is deliberately chosen at the moment right after the pressure perturbation bounce back from the wall, and it is about to spread out towards downstream, and will hit the shock again until dies out. The entropy perturbation do not bounce back [10], instead, it will just damped out in the viscous layer near the wall at further downstream.

The computation of zone 2 is based on using the exit boundary time history of zone 1 as the entrance boundary condition for zone 2 and the freestream perturbation at shock position. While computing zone 1, the exit boundary condition is saved for every 10000 time steps. In zone 2 computation, the discrete zone 1 exit boundary condition at different time are interpolated by using 5^{th} order polynomials. The spatial resolution for zone 2 is $120 \times 120 \times 4$. Figure 42 shows the entropy perturbation passing through the entrance boundary at the left-hand-side, and going to the right; the downstream direction. From Figure 42, the perturbation from the freestream passing into the upper shock boundary is insignificant.

VII. Improvements and Future Works

The development of the computer code for zone 2 to zone 18 is accomplished. The future work is to finish computing all the zones by using this code, and compare the results to Purdue's laser spot Mach 6 wind tunnel experiment results.

There are many aspects of this simulation can be further improved. If the time scale for the diffusion and propagation to take place is not small compare to the length scale of travelling in freestream, then one should perform simulation of the hotspot in freestream before hitting the bow-shock. For the simulation of hotspot, the most important aspect is to simulate the energy propagation and diffusion process, and the weak spherical shock around the thermal core, in high accuracy. To archive that, high spatial resolution is required. Multi-grid method is used to create high resolution throughout the hotspot peak region, since the gradient of temperature or density is spurious. Shock-capturing domain with high-order upwind scheme will be implemented to perform this individual simulation. Using upwind scheme can avoid numerical oscillations when the gradient is too spurious.

As stated previously, the flow variables of the freestream perturbation and their time derivatives are necessary to determine the shock location. One way to find the time derivatives of flow variables is to run the hotspot simulation individually, and save all the data at the shock location for many time steps. Then, use high-order finite difference schemes to determine the time derivatives for all flow variables at the shock location. The disadvantage to this approach is that extremely large computer memory capacity is required.

The other smarter way to find the time derivatives of flow variables is to run the freestream hotspot simulation and behind-shock simulation at the same time, but the time-step differencing between two simulations must be strictly controlled according to the finite difference schemes that are used to determine the time derivatives of the flow variables at the shock location. The advantage to this approach is that the number of time-steps that are needed to be saved from the freestream hotspot simulation is just the number of points that are contained in the finite difference stencil, which is used to compute the time derivatives at the shock location. Hence, the memory requirement is dramatically low.

Moreover, Salyer [3, 4] has presented Gaussian based modeling equations for smoothly modeling the diffusion, propagation and the weak shock in the hotspot. Using Salyer's model to replace the steady Gaussian model in this paper is the simplest way to improve the unsteadiness and physically realistic quality of hotspot in the DNS.

In the future, another case of nose radius equal to 0.0005 m will be computed. Such nose radius is proposed by Schneider for studying boundary layer receptivity with sharper nose effect. Thus, the DNS results can be compared to experiment results to see the effect of various nose bluntness to the boundary layer receptivity.

VIII. Conclusion

In this paper, we have performed mean flow simulation of Purdue's compression cone under their Mach-6 wind tunnel flow conditions. The location of case 2 steady shock front matches well with Purdue's shock-front. The case 2 mean flow results show the adverse pressure gradient presents along the wall of compression cone, and we have performed LST analysis. The case 2 LST results show that the most amplified frequency amongst all five proposed frequencies is 278996 Hz, the N-factor at x=0.4 m is 12.5, and the rest of the frequencies between 271797 Hz and 297494 Hz appear close to Purdue's LST results, for instance, at 0.4 m, the corresponding N-factors are between 11 to 12. Hence, the shock-fitting DNS of the compression cone mean flow can be concluded as consistent to Purdue's shock-capturing DNS results by LST analysis.

We also have validated the computer code and procedures for simulating general unsteady flow by running a 1D sinusoidal entropy disturbance case as a preliminary run for the hotspot case. The hotspot is being modeled as a single 3D entropy pulse with Gaussian equation. The hotspot cases in zone 1 and 2 demonstrate behind shock acoustic and entropy perturbations generated by the interaction of freestream hotspot and shock. We believe that some of the instability perturbation will grow and become the dominant perturbation that causes boundary layer transition at further downstream due to the compression effect along the wall. Therefore, the simulation needs to be performed for the rest of the cone length, so as to verify our hypothesis. In order to produce results that are more comparable to hotspot experiment, the 3D hotspot modeling equation will be modified with a more complex one that includes the effect of diffusion and weak shock propagation of the hotspot in freestream.

Appendix

All the flow variables shown in the figures are dimensionless, which are normalized by the corresponding freestream values.

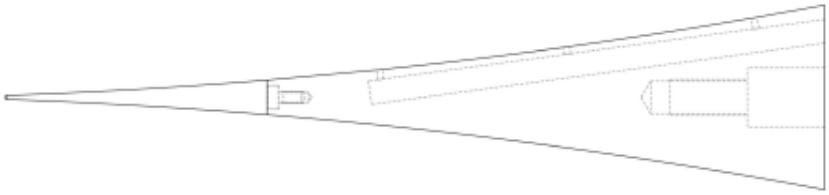

Figure 1. Schematic diagram of Purdue's Compression Cone [5]

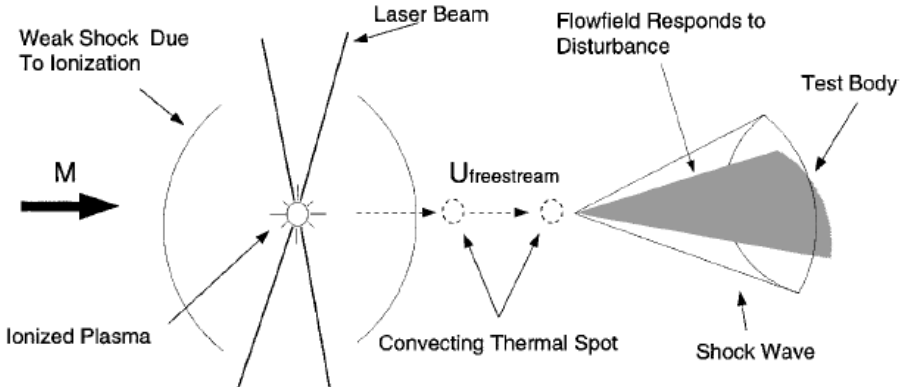

Figure 2. Schematic explanation of the laser-spot and cone scenario. [9]

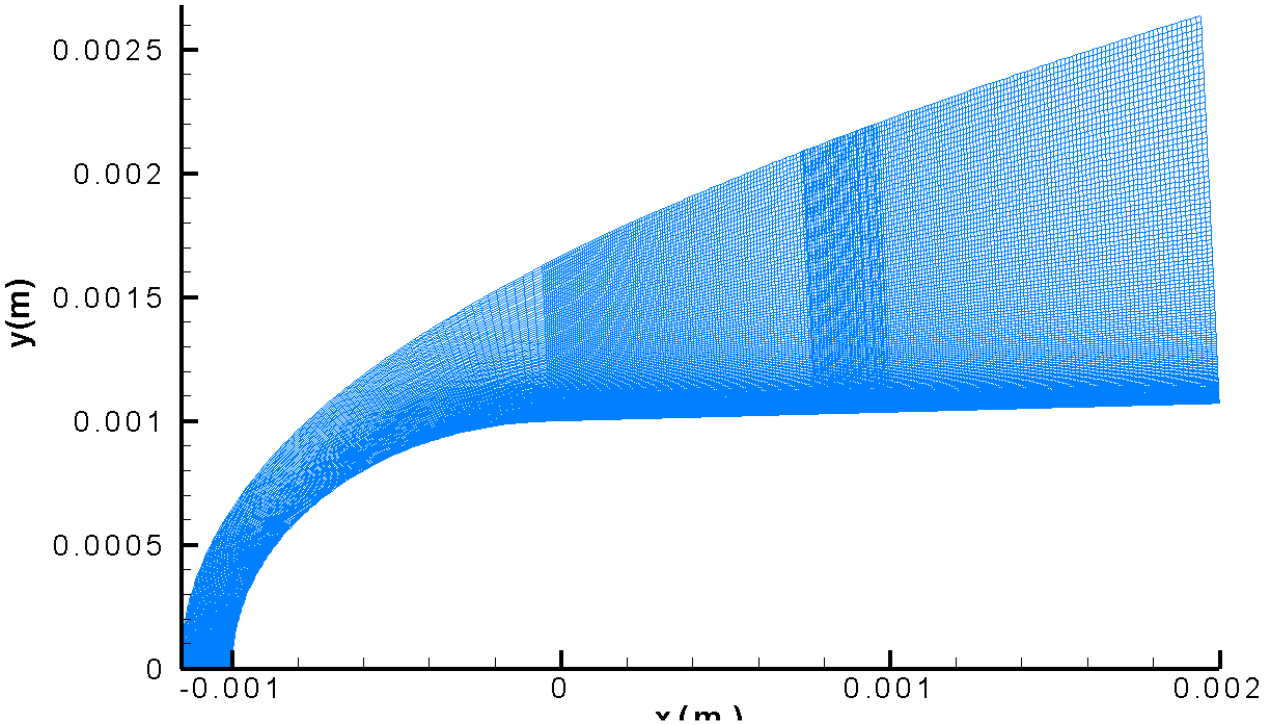

Figure 3. Partial view of grid configuration in zone 1, 2&3.

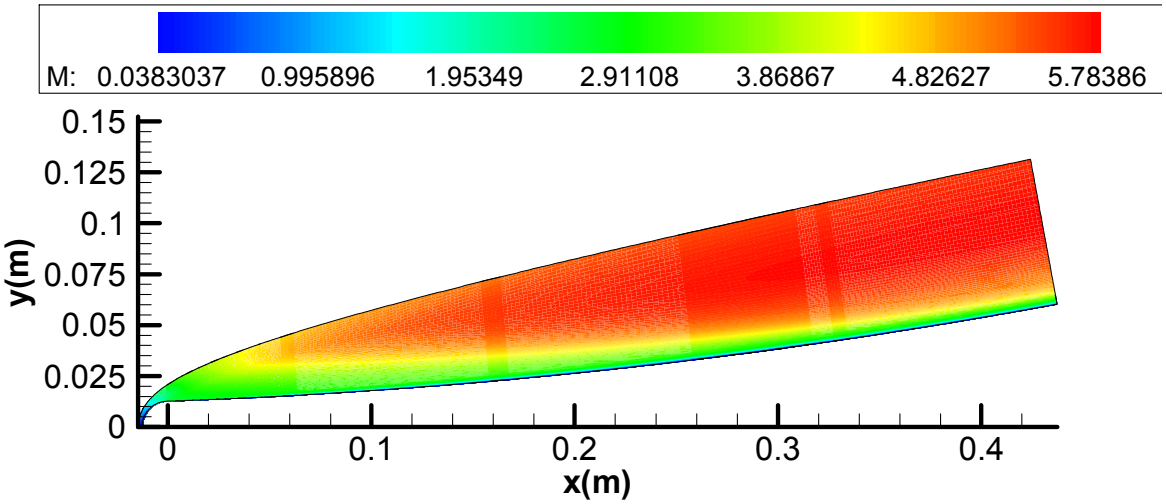

Figure 4. Steady flow Mach number contour plot of Case1.

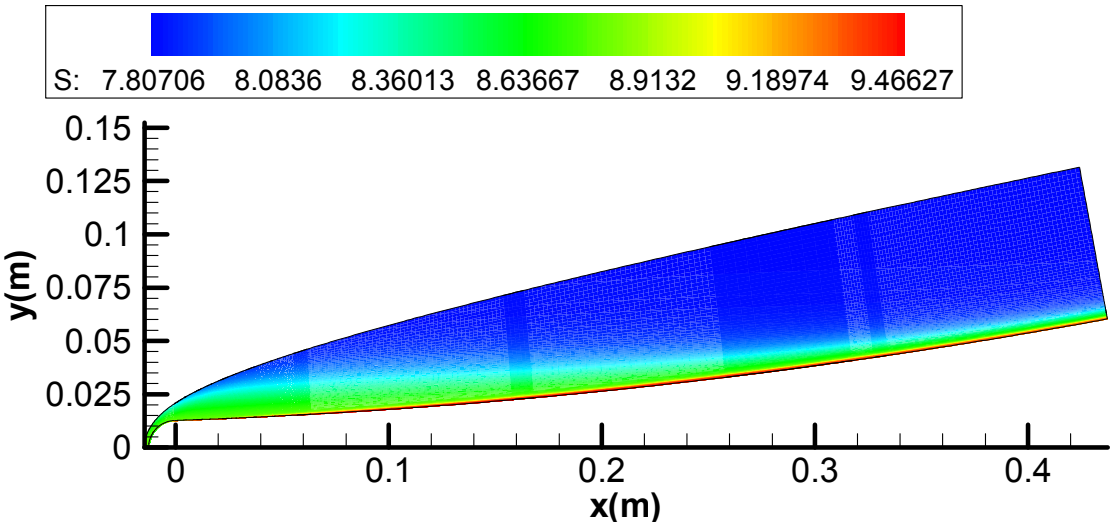

Figure 5. Steady flow entropy contour plot of Case1.

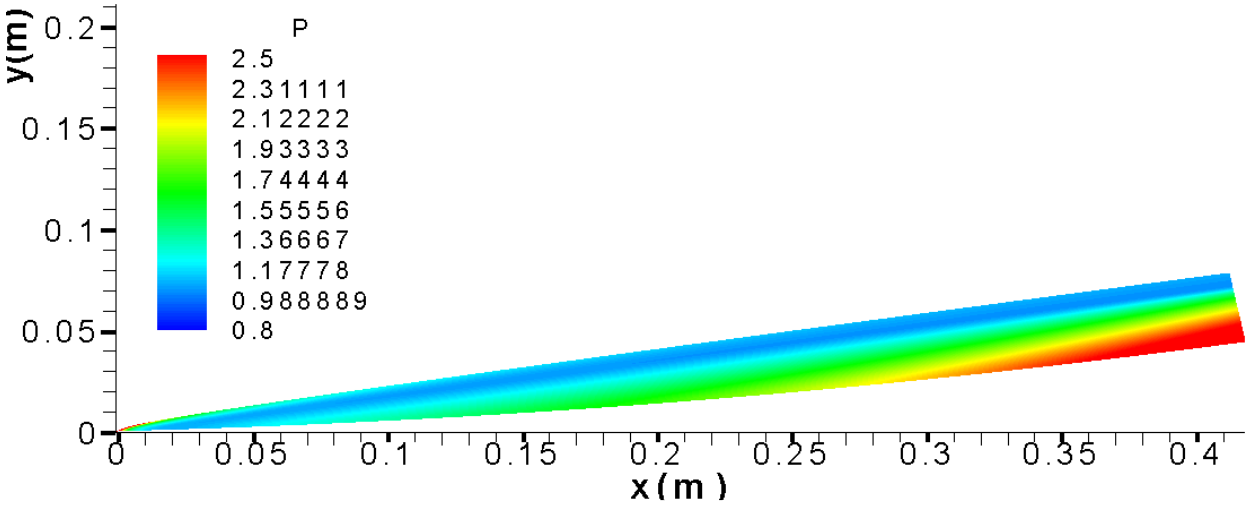

Figure 6. Contour of non-dimensional pressure in case 2

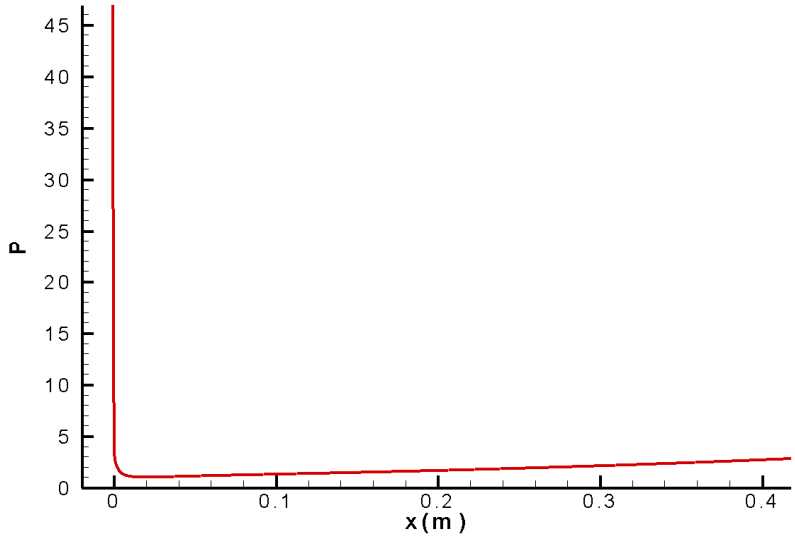

Figure 7. Pressure along the wall in case 2

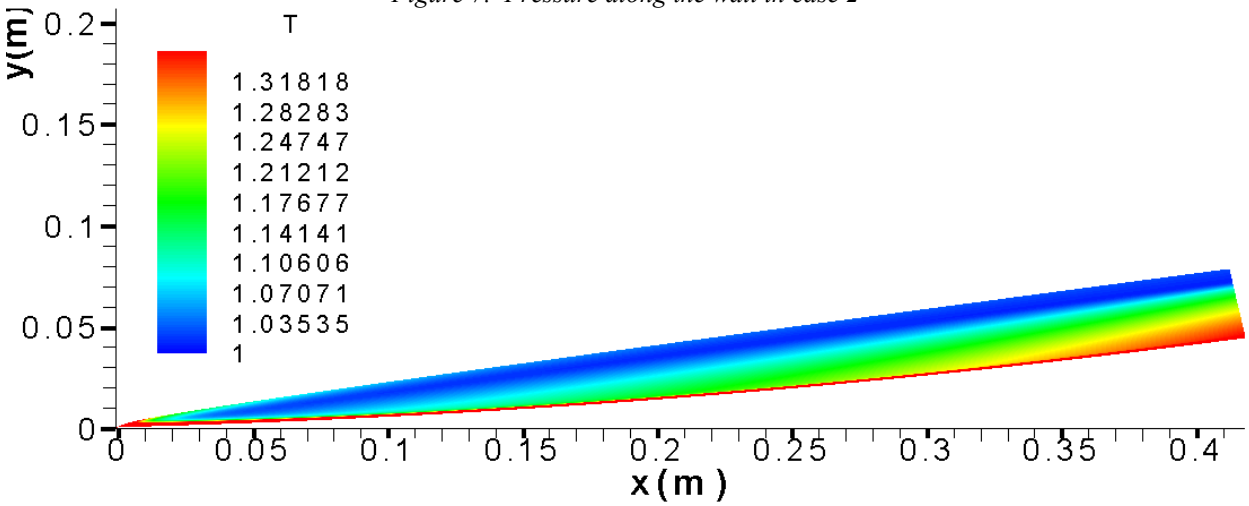

Figure 8. Contour of non-dimensional temperature in case 2

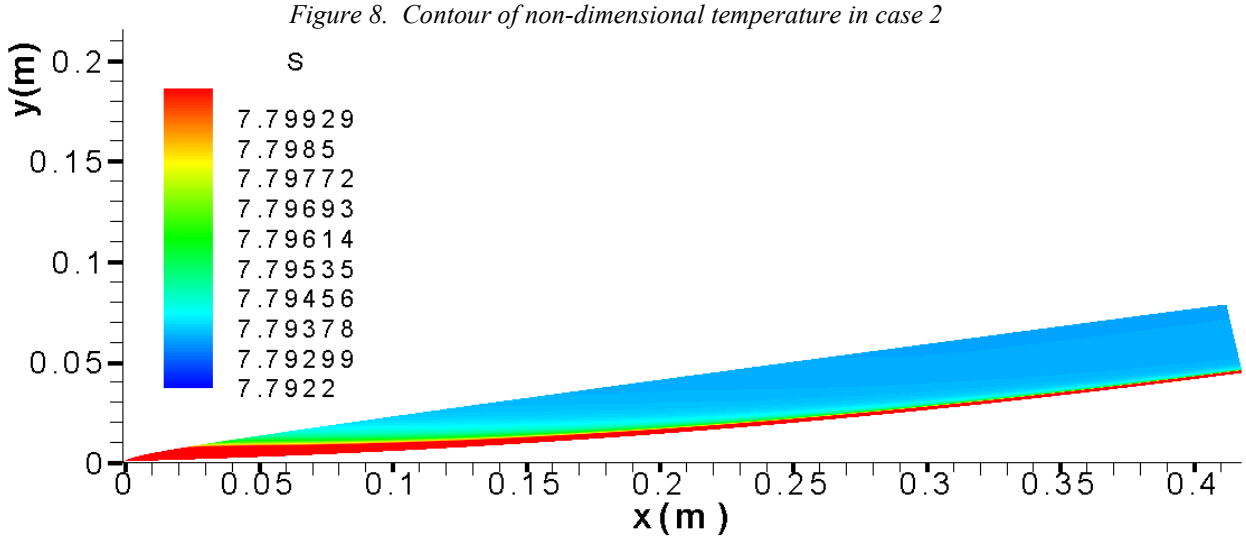

Figure 9. Contour of non-dimensional entropy in case 2

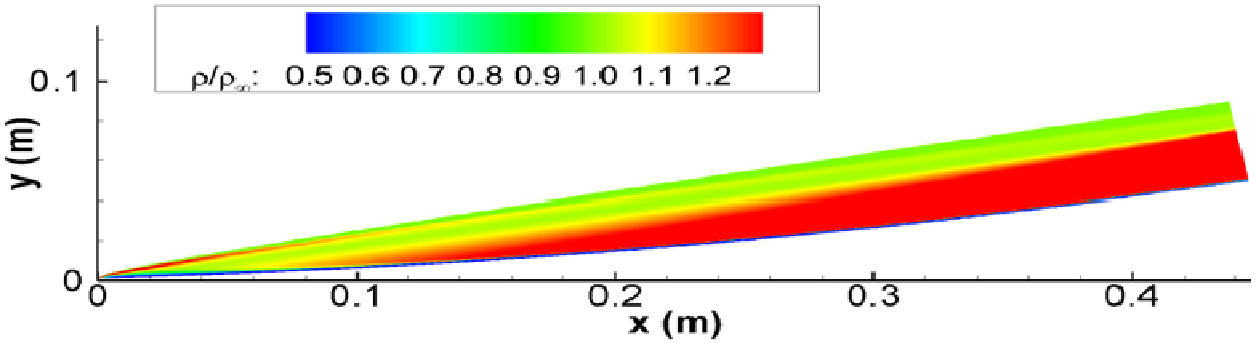

Figure 10. Purdue's non-dimensional density contour plot [5]

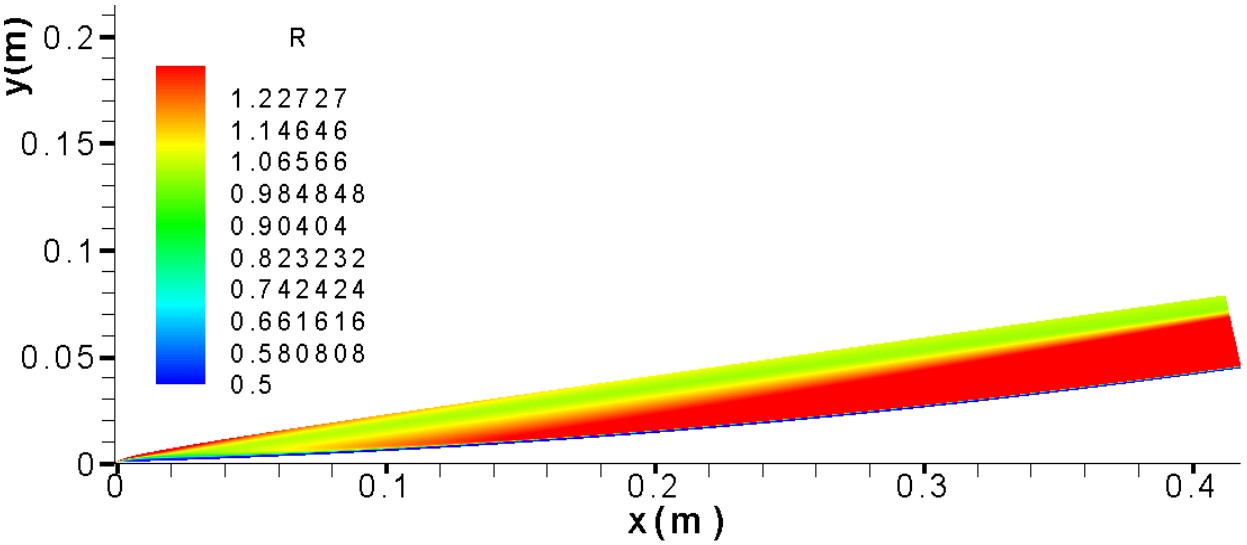

Figure 11. Case 2 non-dimensional density contour plot

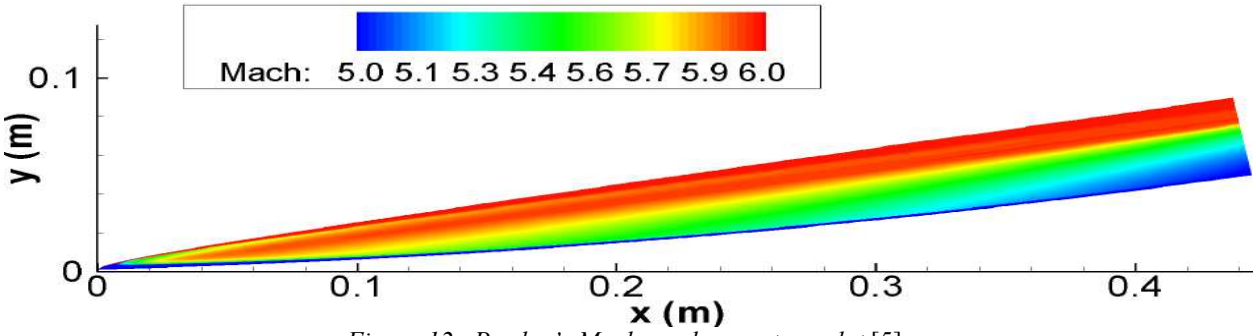

Figure 12. Purdue's Mach number contour plot [5]

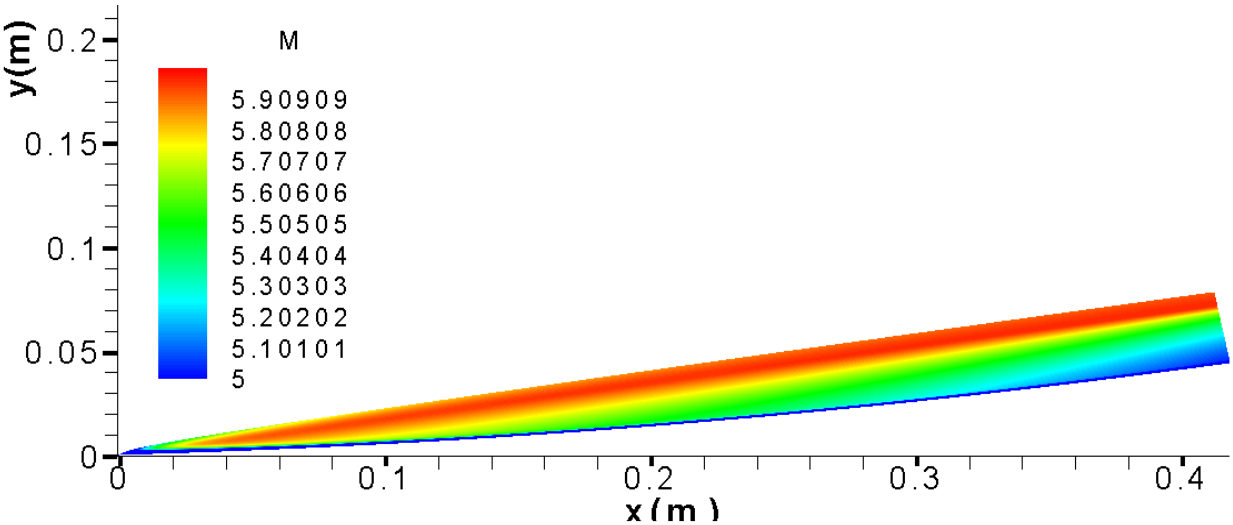

Figure 13. Case 2 Mach number contour plot

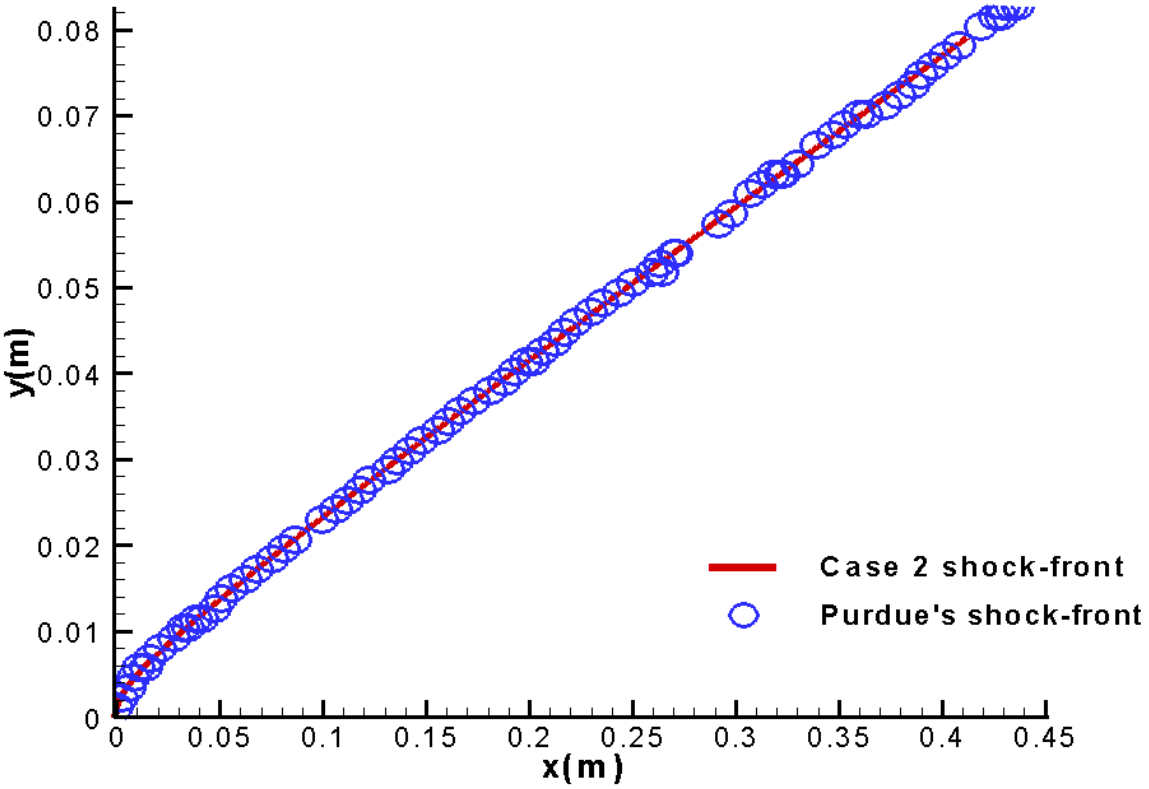

Figure 14. Comparison of shock front location

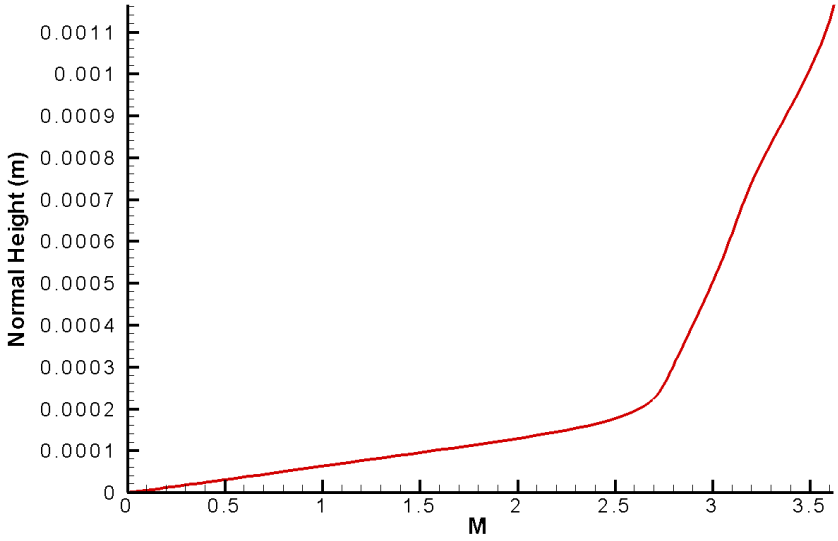

Figure 15. Mach number profile of case 2 at x=0.001m

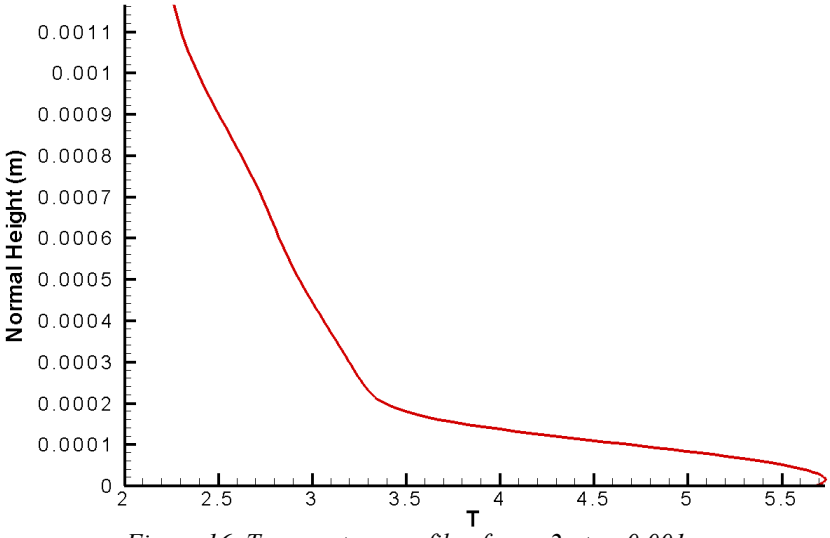

Figure 16. Temperature profile of case 2 at x=0.001m

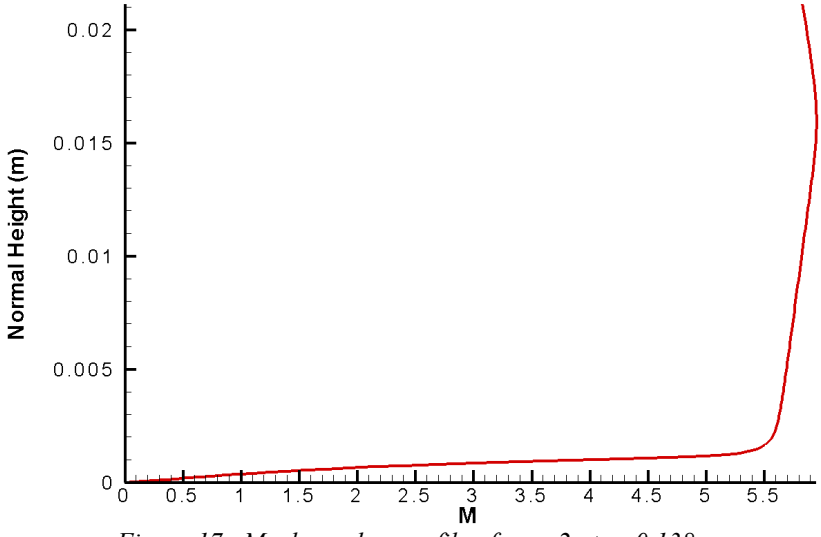

Figure 17. Mach number profile of case 2 at x=0.138m

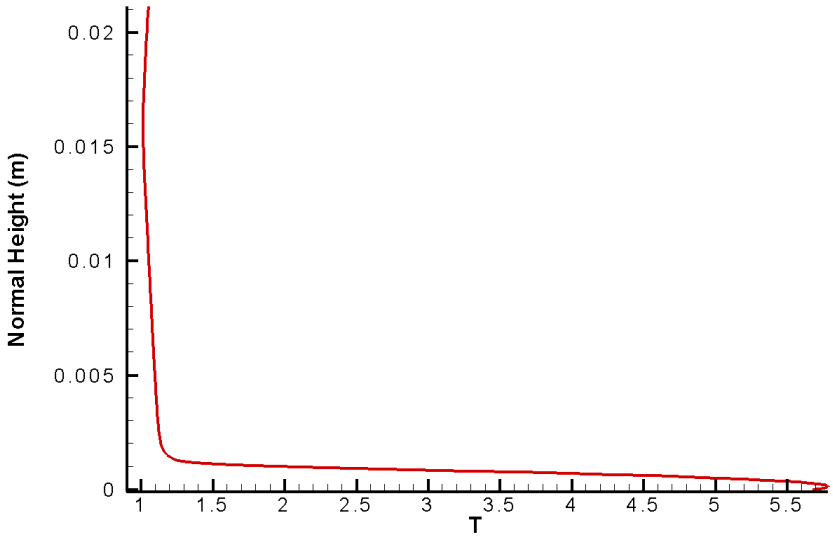

Figure 18. Temperature profile of case 2 at x=0.138m

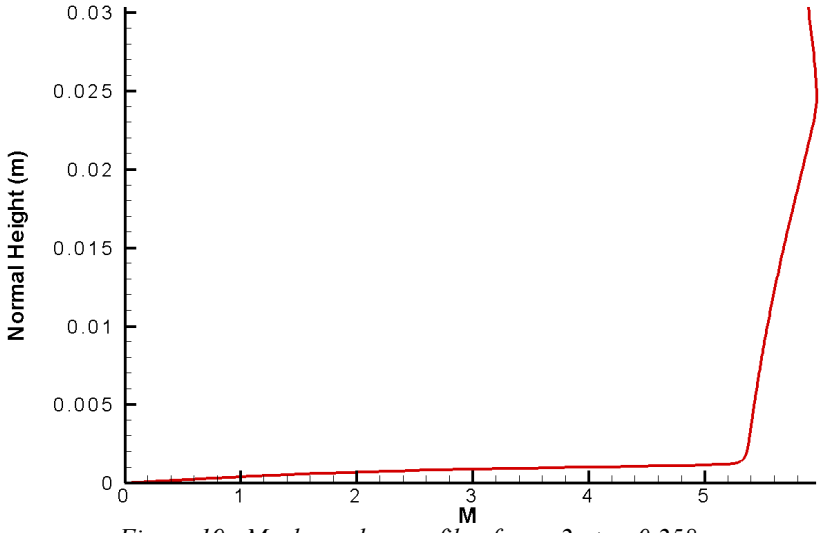

Figure 19. Mach number profile of case 2 at x=0.258m

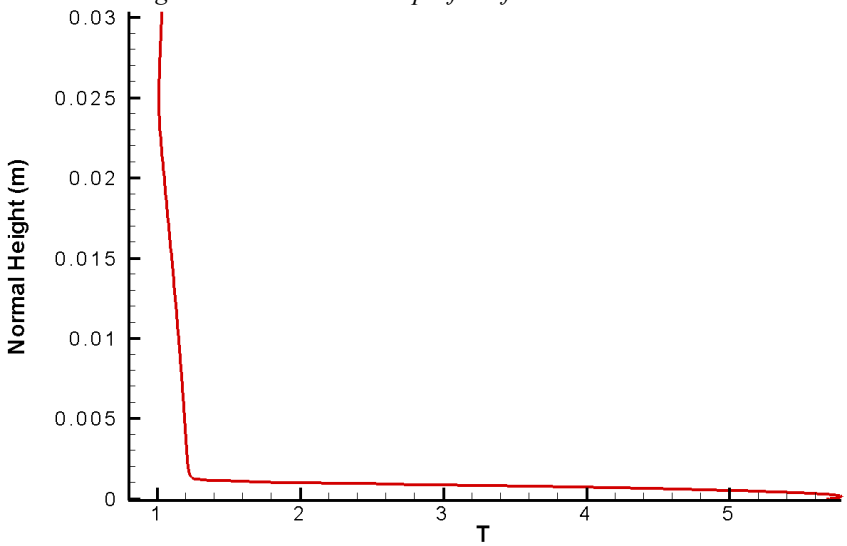

Figure 20. Temperature profile of case 2 at x=0.258m

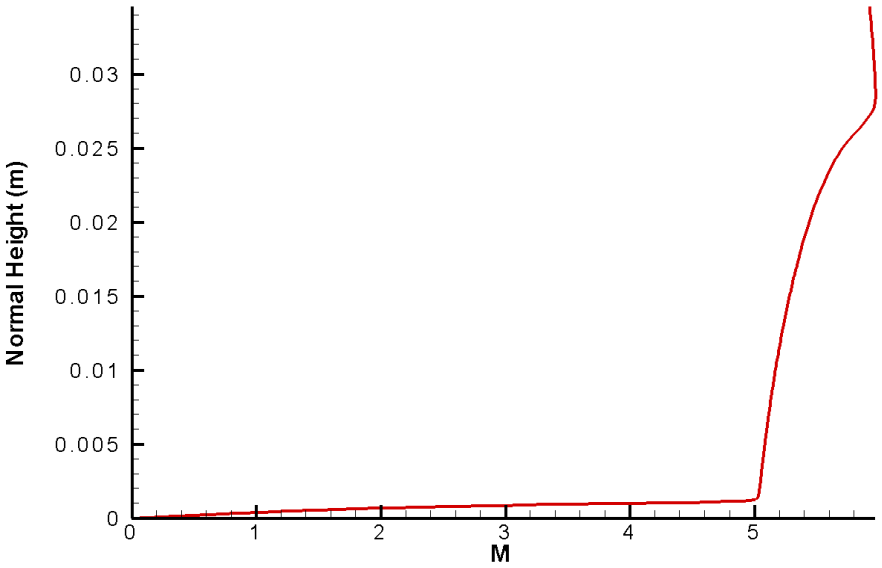

Figure 21. Mach number profile of case 2 at x=0.418m

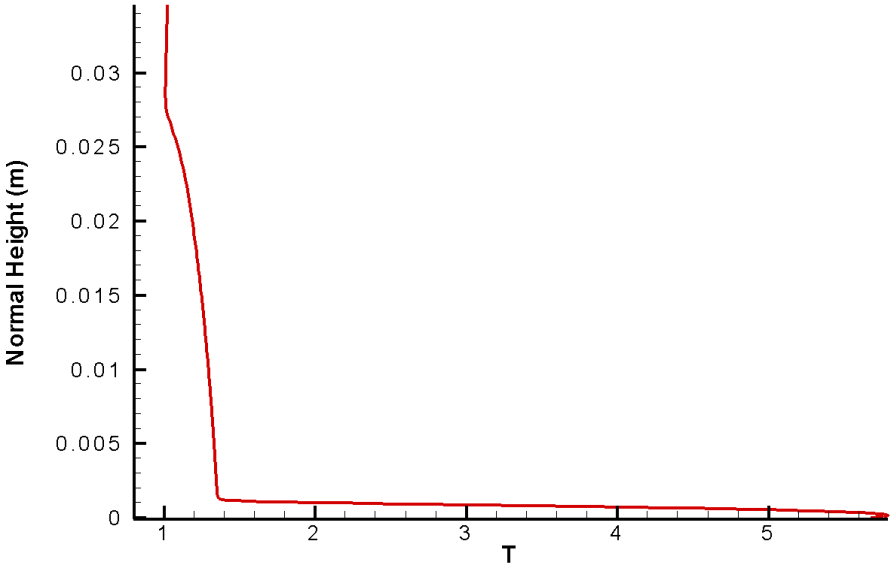

Figure 22. Temperature profile of case 2 at x=0.418m

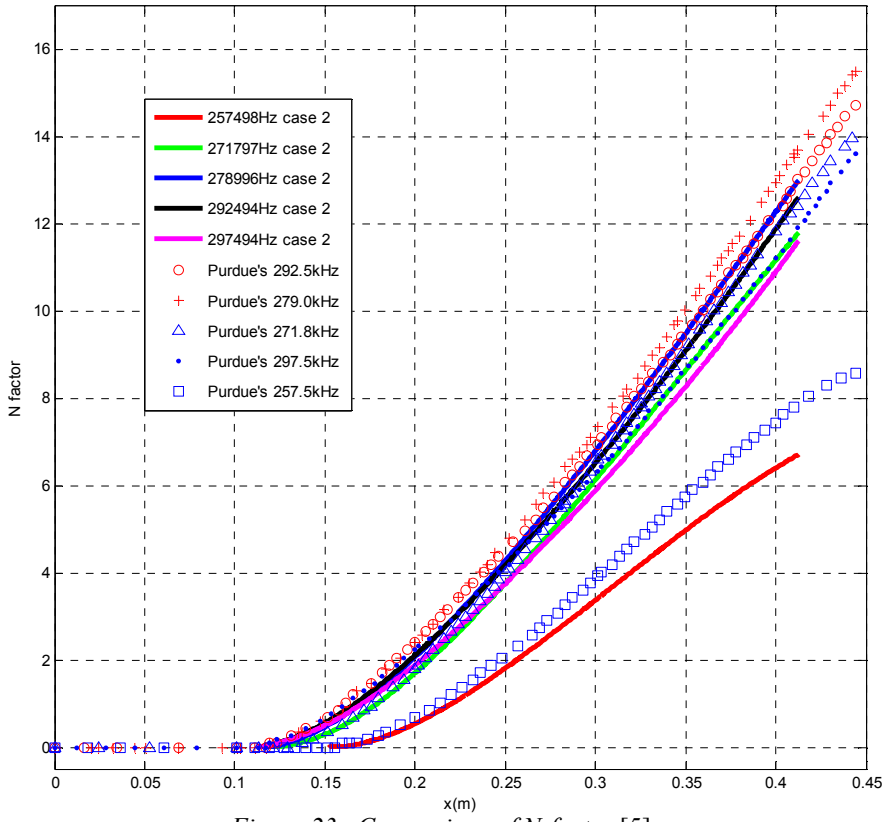

Figure 23. Comparison of N-factor [5]

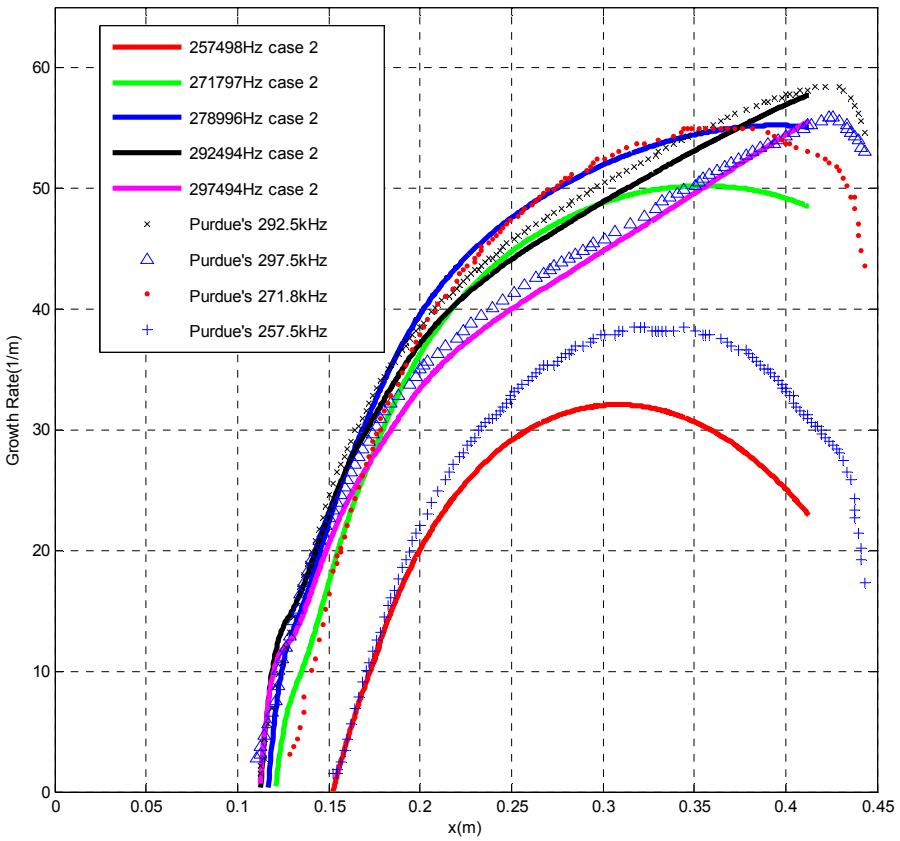

Figure 24. Comparison of growth rate [5]

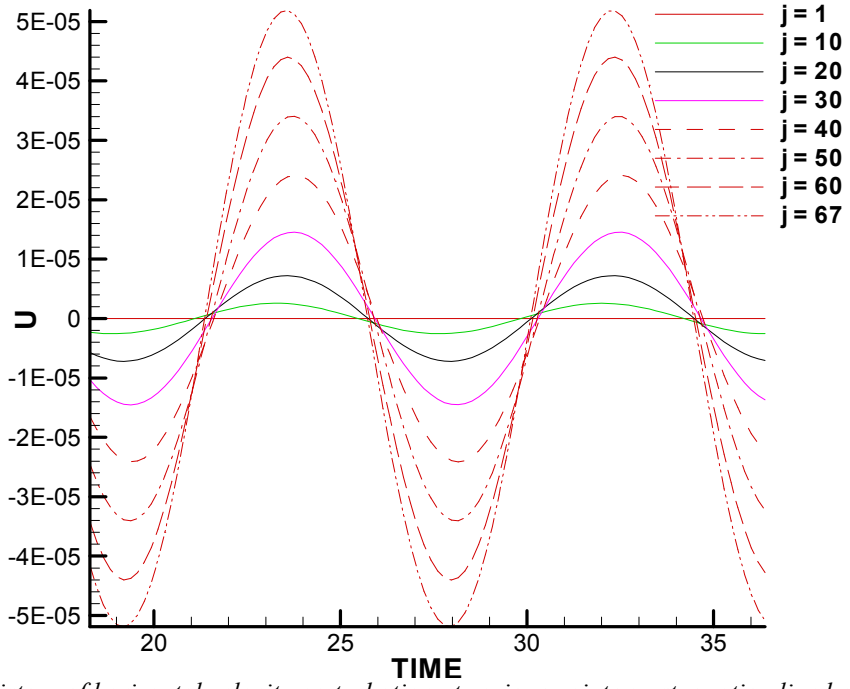

Figure 25. Time history of horizontal velocity perturbation at various points on stagnation line behind shock nearby the wall(zone 1)

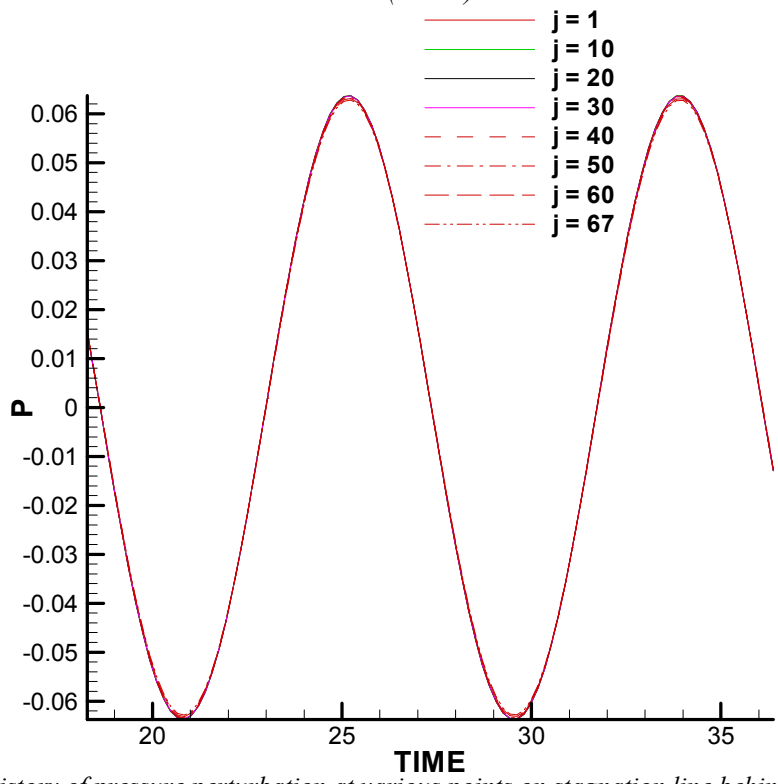

Figure 26. Time history of pressure perturbation at various points on stagnation line behind shock nearby the wall(zone 1)

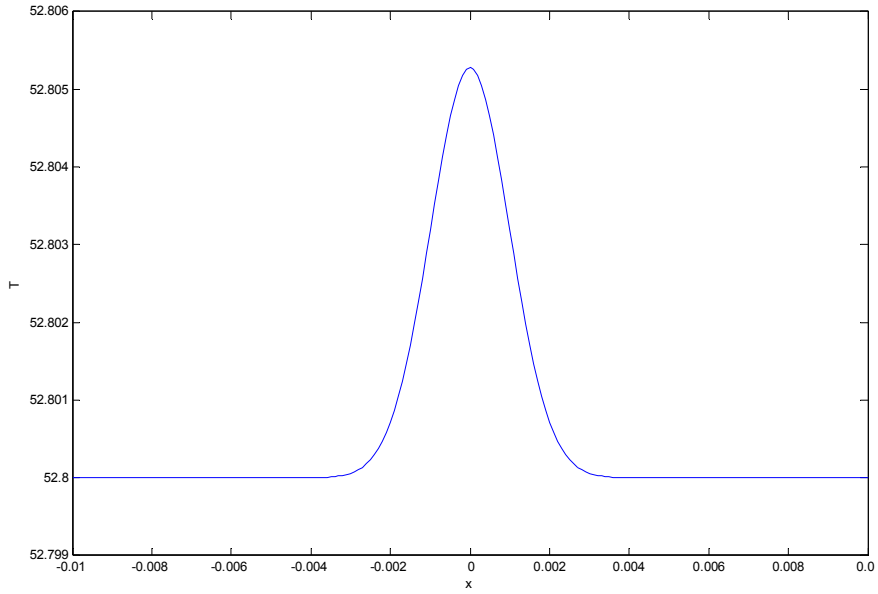

Figure 27. Gaussian distribution of perturbed temperature in radial-direction (case A)

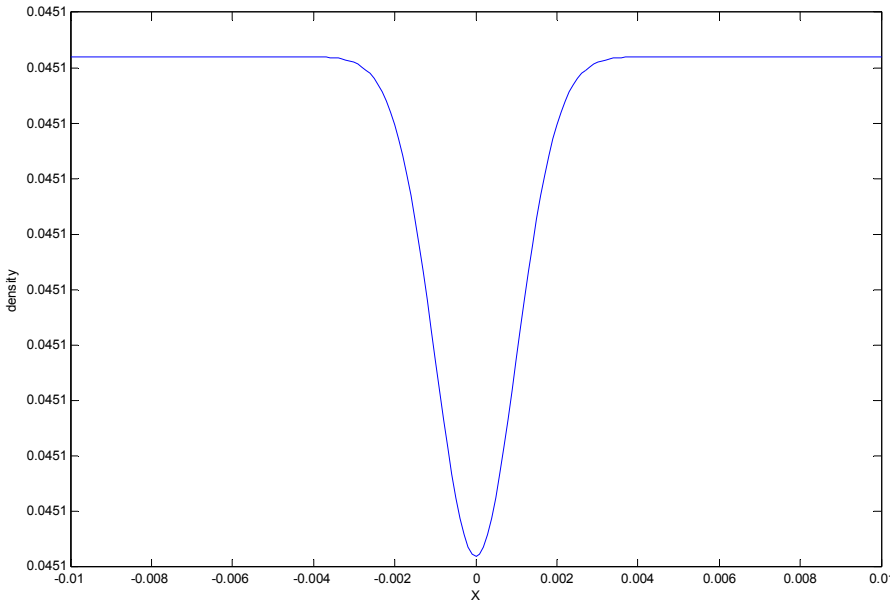

Figure 28. Gaussian distribution of perturbed density in radial-direction (case A)

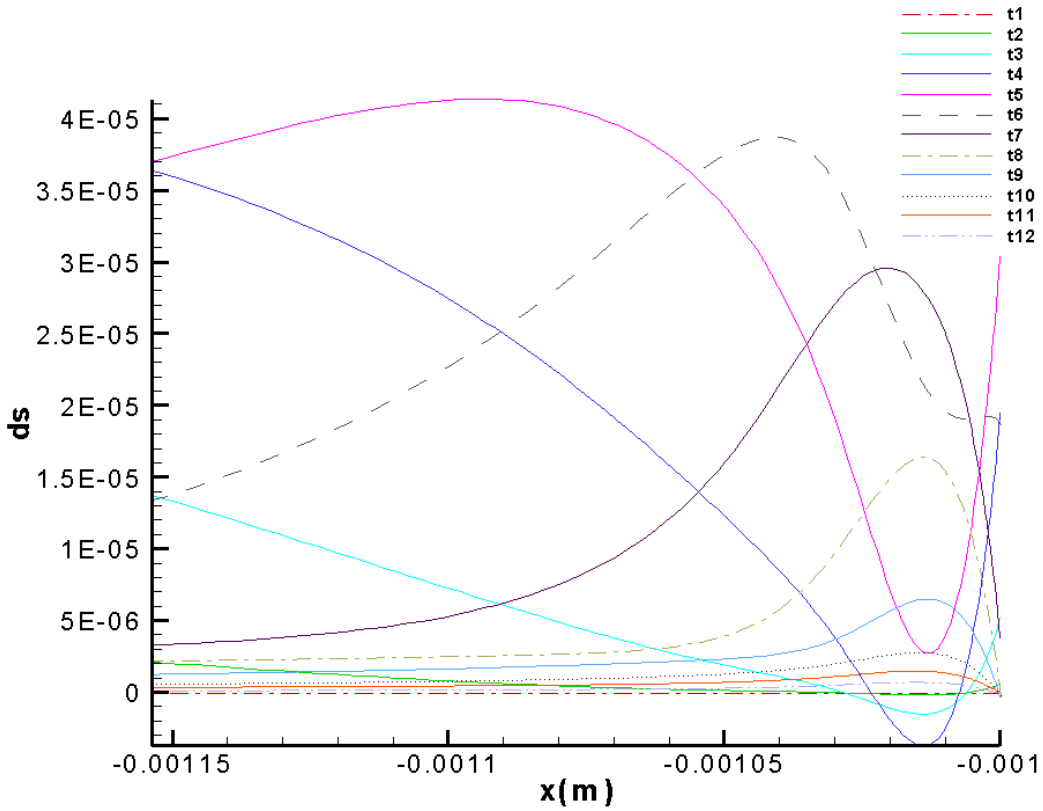

Figure 29. Entropy perturbation on stagnation line behind the shock at various time (case A, zone 1)

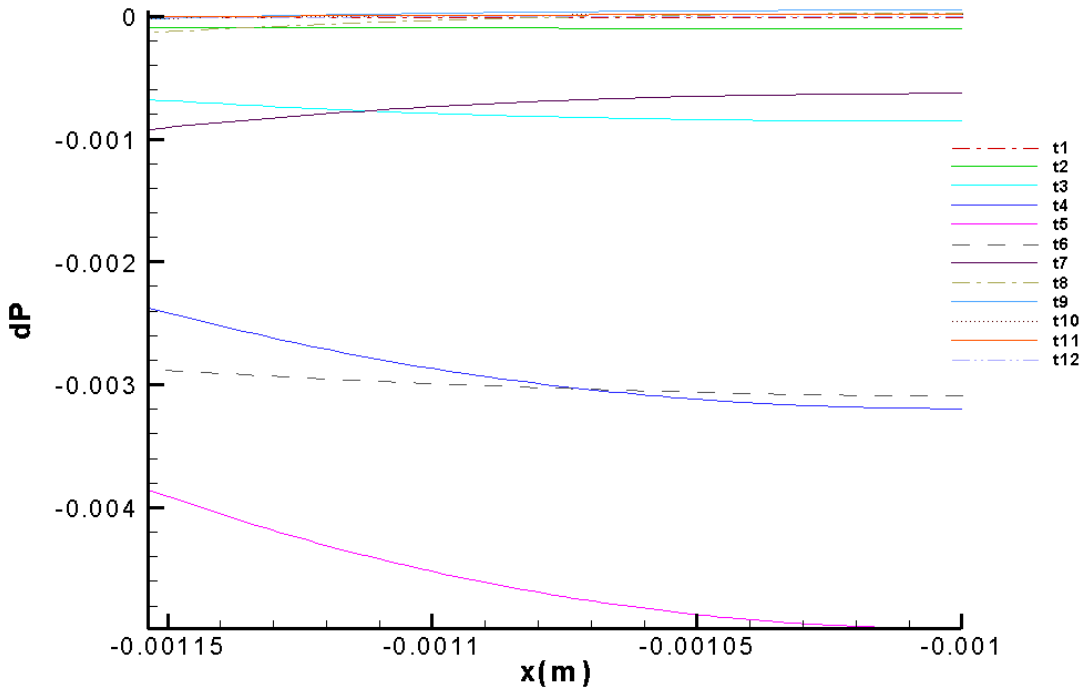

Figure 30. Pressure perturbation on stagnation line behind the shock at various time (case A, zone 1)

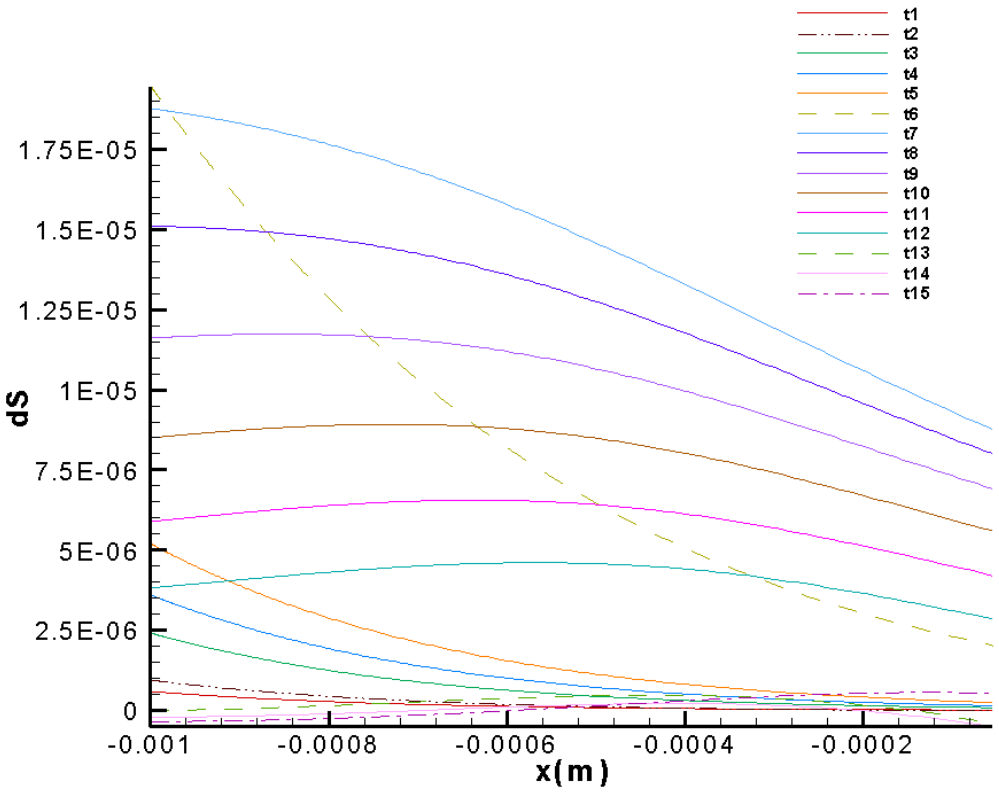

Figure 31. Entropy perturbation along wall surface at various time (case A, zone 1)

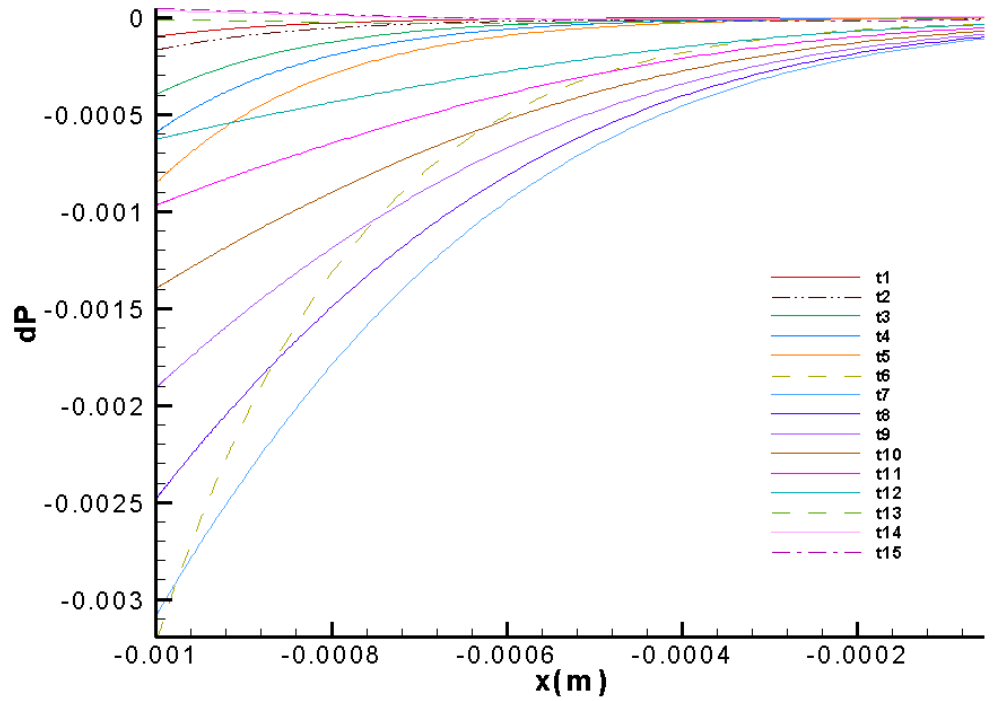

Figure 32. Pressure perturbation along wall surface at various time (case A, zone 1)

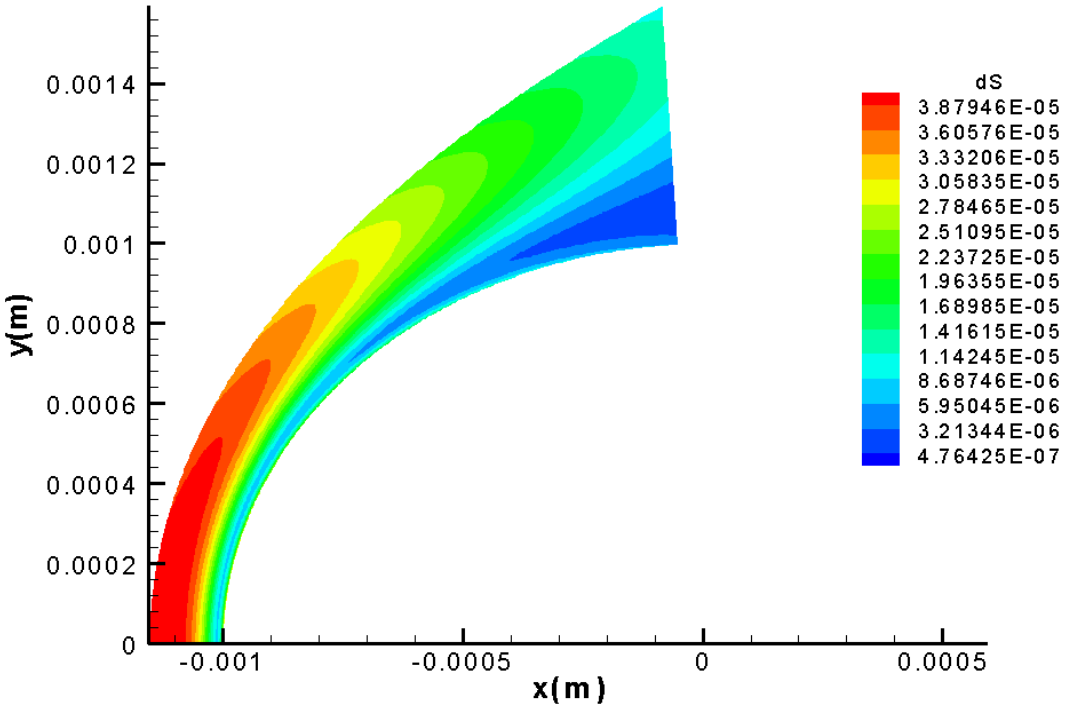

Figure 33. Contour plot of hotspot entropy perturbation behind the shock in case A, zone 1

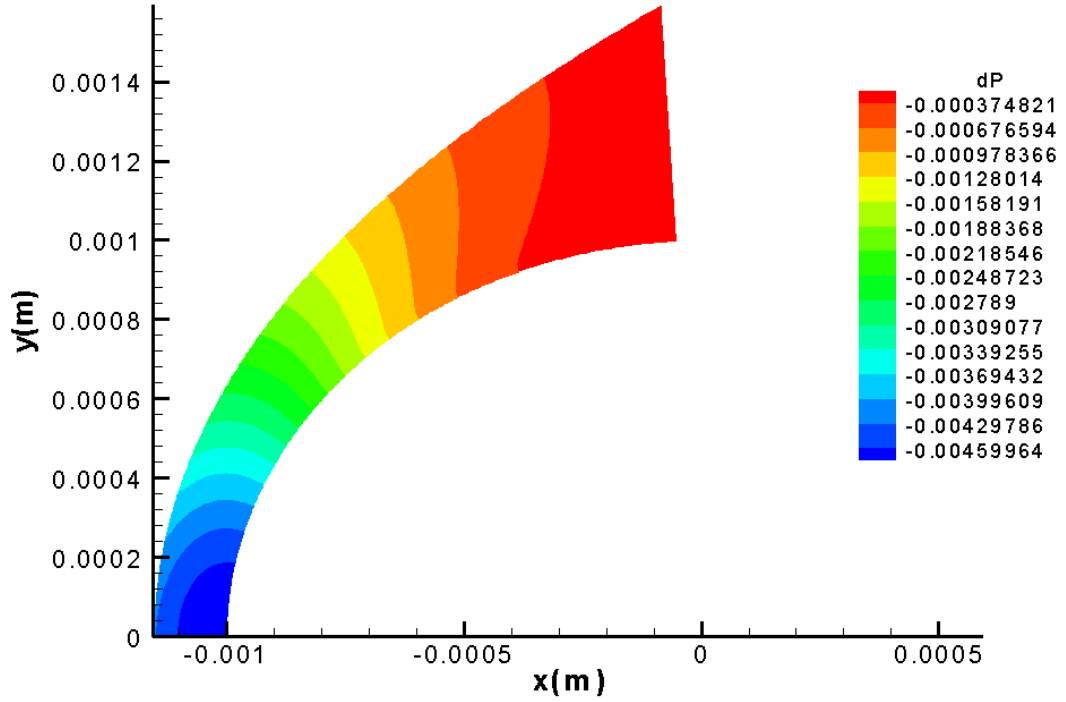

Figure 34. Contour plot of hotspot pressure perturbation behind the shock in case A, zone 1

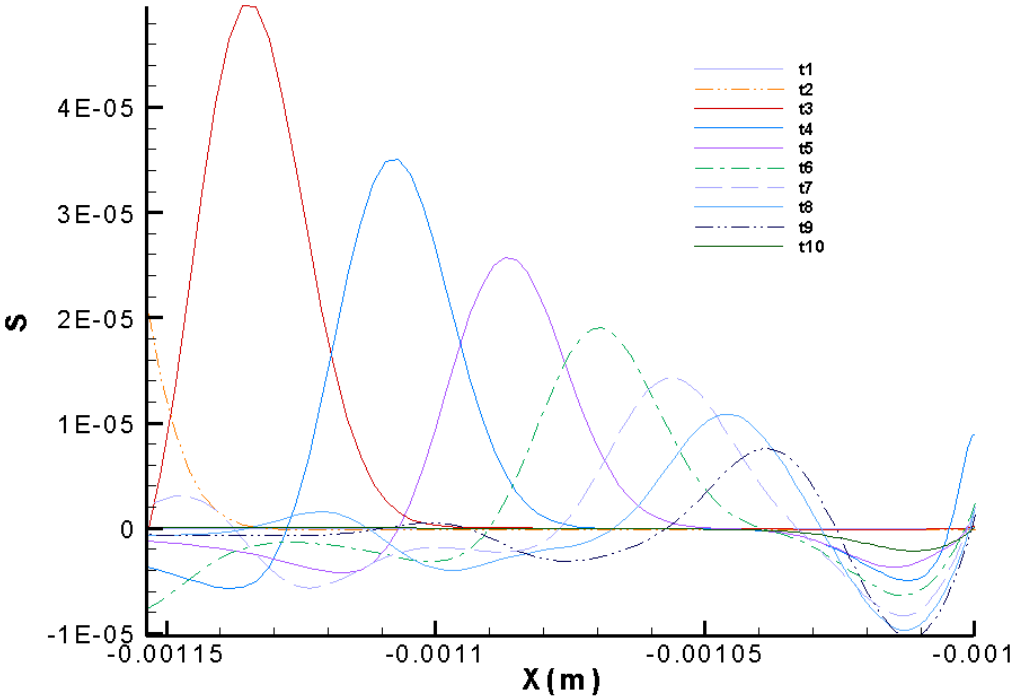

Figure 35. Entropy perturbation on stagnation line behind the shock at various time (caseB, zone 1)

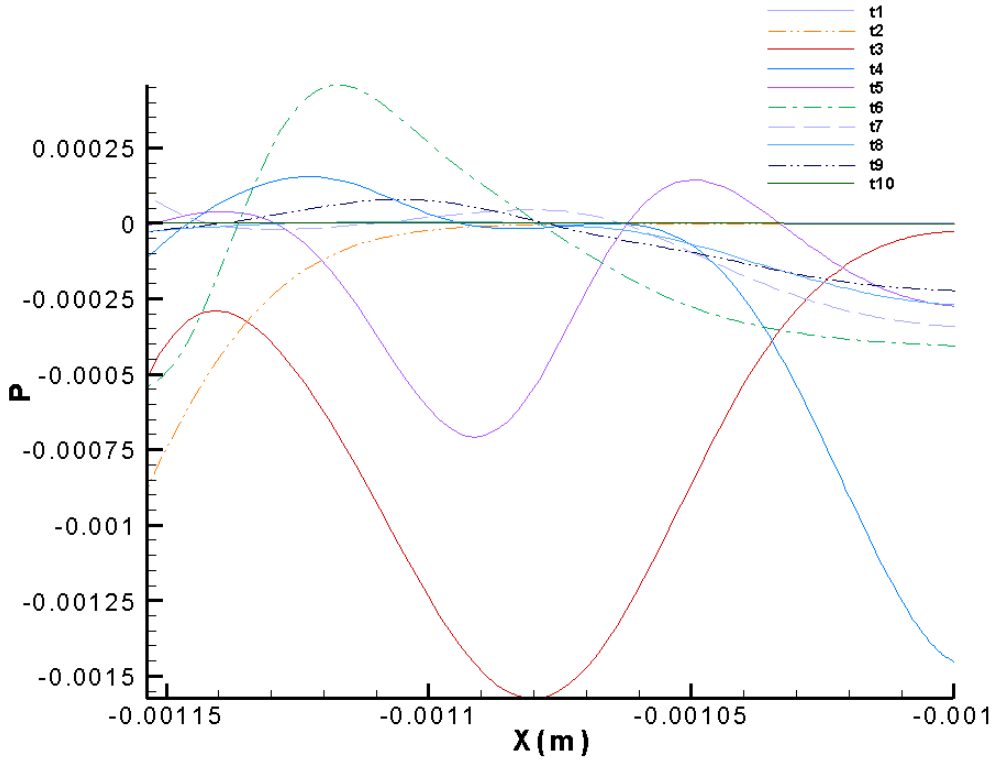

Figure 36. Pressure perturbation on stagnation line behind the shock at various time (case B, zone 1)

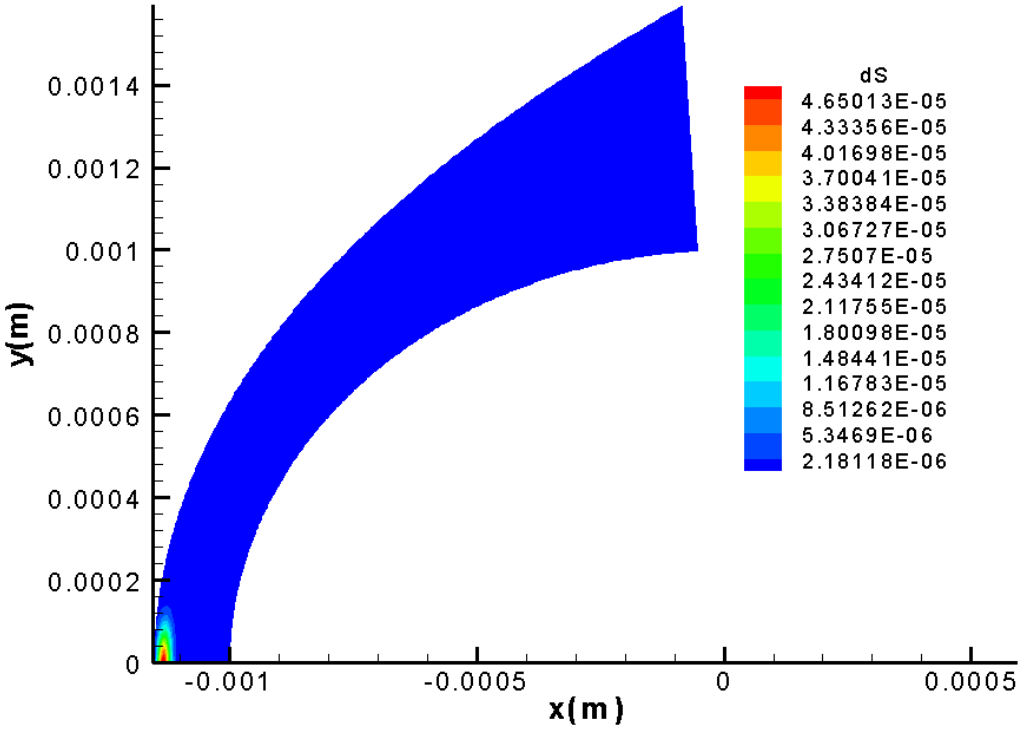

Figure 37. Contour plot of hotspot entropy perturbation behind the shock in case B, zone 1

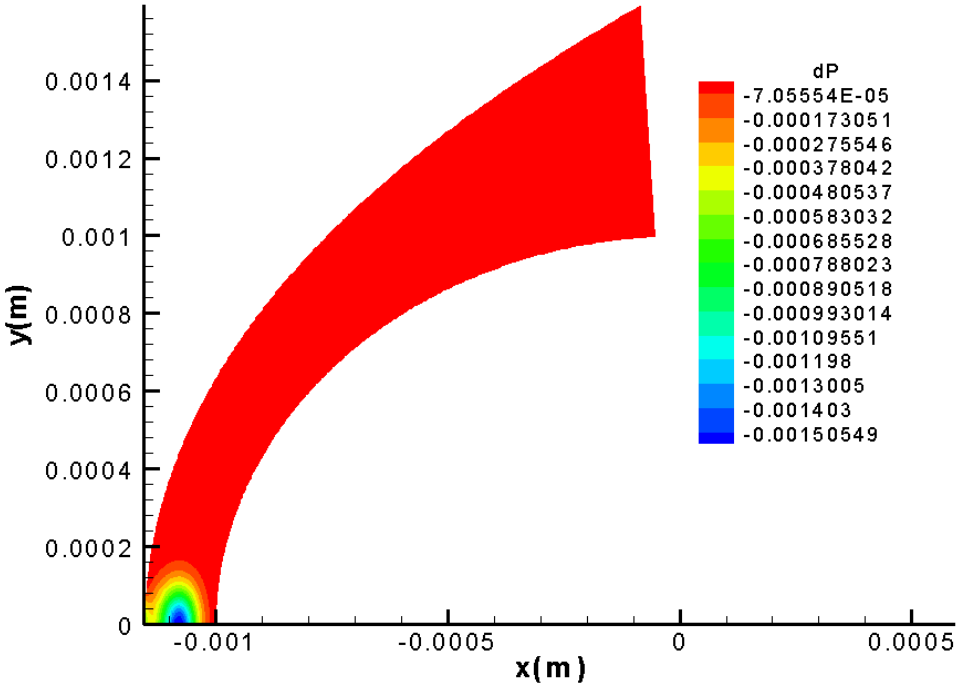

Figure 38. Contour plot of hotspot pressure perturbation behind the shock in case B, zone 1

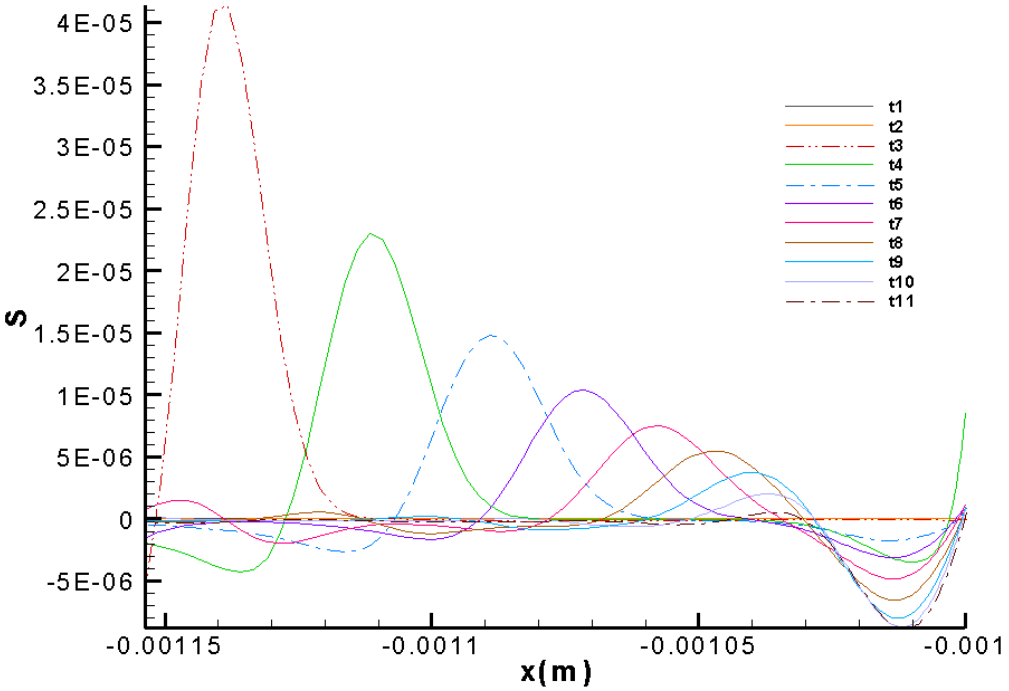

Figure 39. Entropy perturbation on stagnation line behind the shock at various time (case C, zone 1)

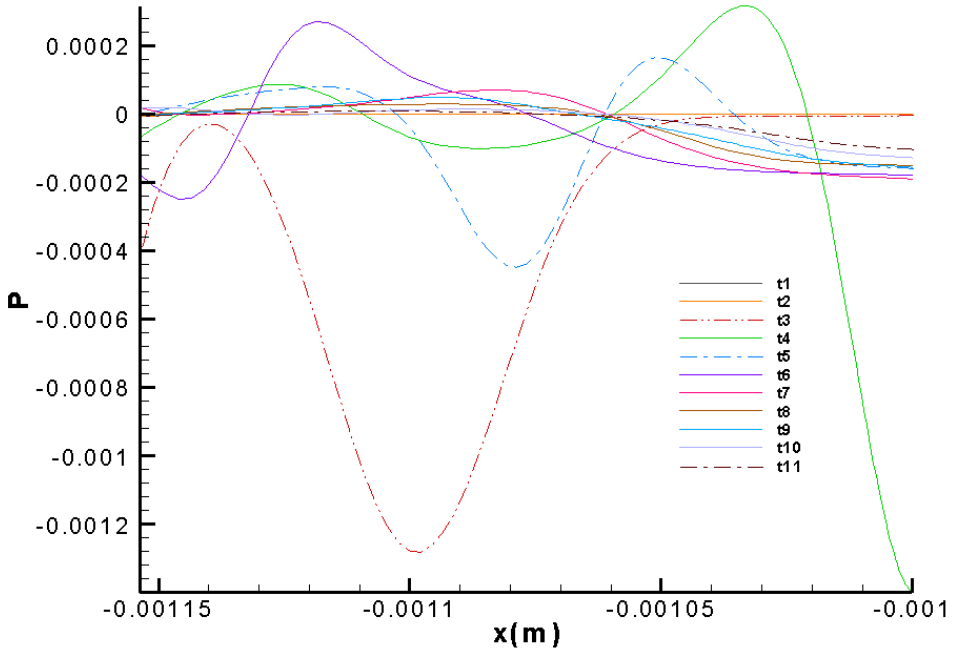

Figure 40. Pressure perturbation on stagnation line behind the shock at various time (case C, zone 1)

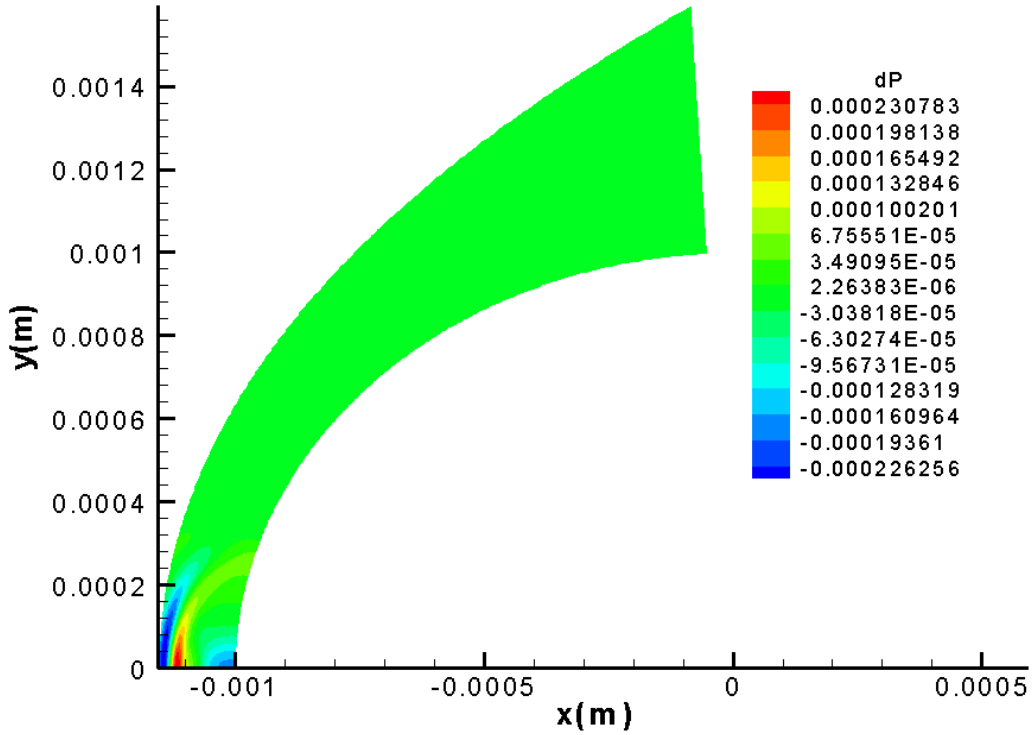

Figure 41. Contour plot of hotspot pressure perturbation behind the shock in case C, zone 1

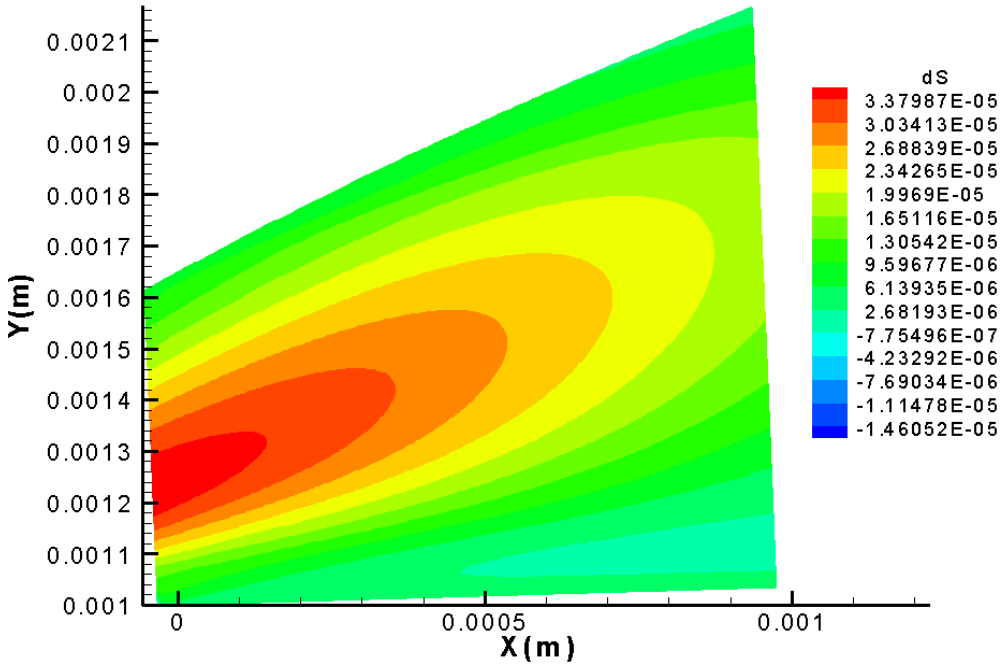

Figure 42. Contour plot of hotspot entropy perturbation behind the shock in case A, zone 2

Acknowledgments

This work was sponsored by the AFOSR/NASA National Center for Hypersonic Research in Laminar-Turbulent Transition and by the Air Force Office of Scientific Research, USAF, under Grant No. FA9550-07-1-0414, monitored by Dr. John Schmisseur. The views and conclusions contained herein are those of the authors and should not be interpreted as necessarily representing the official policies or endorsements either expressed or implied, of the Air Force Office of Scientific Research or the U.S. Government.

The first author of this paper specially would like to thank Jia Lei for providing assistance in LST, also would like to thank the valuable advising and mentoring from the senior members in UCLA hypersonic CFD group of year 2010. Both authors of this paper specially thank to Professor Steve Schneider at Purdue University and his group for providing the data and information of their compression cone wind-tunnel experiment, which make the authors' work more comparable to the real-world experiments.

References

[1] Dunn, J.W., "Numerical Simulation of Bow-Shock/Disturbance Interactions in Mach-4 Flows Past a Hemisphere" AIAA Paper, 98-0007, January 1998.

[2] Reshotko E., "Hypersonic Stability and Transition", Hypersonic Flows for Reentry Problems, Berlin: Springer, 1991.

[3] Salyer, T.R., "Laser Differential Interferometry for Supersonic Blunt Body Receptivity Experiments", PhD Thesis, Purdue University, May 2002.

[4] Salyer, T.R., Collicott, S.H., Schneider, S.P., "Characterizing Laser-Generated Hot Spots for Receptivity Studies", AIAA Journal, Vol.44, No.12, December 2006.

[5] Schneider, S.P., Wheaton, B.M., Julinao, T.J., Berridge, D.C., Chou, A., Gilbert P.L., Casper. K.M., Steen, L.E., "Instability and Transition Measurements in the Mach-6 Quiet Tunnel", AIAA Paper, 2009-3559, June 2009.

[6] Zhong, X. "High-Order Finite-Difference Schemes for Numerical Simulation of Hypersonic Boundary-Layer Transition", Journal of Computational Physics 144,662-709, April 1998.

[7] Zhong, X., "Receptivity of Mach 6 Flow over a Flared Cone to Freestream Disturbance", AIAA Paper, 2004-253, January 2004.

[8] Zhong, X., Lee, T.K., "Nonequilibrium Real-Gas Effects on Disturbance/Bow Shock Interaction in Hypersonic Flow Past a Cylinder", AIAA, 1996.

[9] Schneider, S.P., Collicott, S.H., Schmisseur, J.D., "Laser-Generated Localized Freestream Perturbations in Supersonic and Hypersonic Flows", AIAA Journal, Vol.38, No. 4, April 2000.

[10] McKenzie, J. F., Westphal, K. O., "Interaction of Linear Waves with Oblique Shock Waves", The Physics of Fluids, Vol. 11, No. 11, November 1968.

[11] Kovasznay, L. S. G., "Turbulence in Supersonic Flow", Journal of the Aeronautical Sciences, Vol. 20, No. 10, pp. 657-682, October 1953.

[12] Malik, M. R., "Numerical Method for Hypersonic Boundary Layer Stability", Journal of Computational Physics, 86, 376-413, 1990.